

공학박사 학위논문

# **Graphene-Based Energy Storage Materials as Anodes for Lithium-Ion Batteries**

리튬이차전지 음극용 그래핀 기반의  
나노복합체에 대한 연구

2018년 8월

서울대학교 융합과학기술대학원

융합과학부 나노융합전공

성 채 용

# Graphene-Based Energy Storage Materials as Anodes for Lithium-Ion Batteries

지도 교수; 박 원 철

이 논문을 공학박사 학위논문으로 제출함  
2018년 5월

서울대학교 융합과학기술대학원  
융합과학부 나노융합전공  
성 채 용

성채용의 공학박사 학위논문을 인준함  
2018년 7월

위 원 장 \_\_\_\_\_ (인)

부위원장 \_\_\_\_\_ (인)

위 원 \_\_\_\_\_ (인)

위 원 \_\_\_\_\_ (인)

위 원 \_\_\_\_\_ (인)

## **Abstract**

# **Graphene-Based Energy Storage Materials as Anodes for Lithium Ion Batteries**

Chae-Yong Seong

Program in Nano Science and Technology

Graduate School of Convergence Science & Technology

Seoul National University

Graphene, a one-atom layer and two-dimensional (2D) structure of  $sp^2$ -bonded carbon, has been considered as an ideal candidate for energy storage, especially lithium ion batteries (LIBs) because it possesses high conductivity, large specific surface area, great mechanical strength, low weight, chemically inert and low price. Furthermore, graphene is facile to be chemically functionalized, called graphene oxide (GO) which is typically prepared from graphite to

graphite oxide by oxidization and to GO by subsequent exfoliation. For those reasons, various graphene-based materials have been developed for and applied in LIBs in order to ameliorate the rate capability, overall capacity and so on over the last decade.

Nanomaterial consists of particles or constituents with nanoscale dimensions, usually 1 to 100 nm, or is produced by nanotechnology. The nanomaterial has a significant potential to make a huge impact on the performance of LIBs. The advantages of nanomaterials are better accommodation for the structural strain caused by lithium insertion/extraction, high charge/discharge rates by the extensive electrode/electrolyte interface and short distances for  $\text{Li}^+$  and electron transport. On the other hand, nanomaterials have also disadvantages such as undesirable side reactions on the electrode/electrolyte interface, resulting in self-discharge, poor cyclability and low volumetric energy density for the same mass of micrometer-sized particles and complex synthesis of nanoparticles with dimension control. To complement these drawbacks, graphene is regarded as an effective host material to enhance the electrochemical capability. In LIBs, graphene-based nanomaterials are expected to be alternative and promising anode materials.

This dissertation is the introduction to graphene-based anode nanomaterials relating to graphene paper, metal oxide/graphene composite and metal oxide on graphene. First of all, graphene paper which is hierarchically intercalated with  $\text{Mn}_3\text{O}_4$  nanorods ( $\text{Mn}_3\text{O}_4$  NRs) is fabricated and applied to an anode material in LIBs. In an electrode, graphene functions as a buffer layer for volume expansion of  $\text{Mn}_3\text{O}_4$  NR during Lithium insertion/extraction and the pathway for Li ion and electron transport. In addition,  $\text{Mn}_3\text{O}_4$  NR also plays a crucial role in delivering electrons and Li ions within a paper. A  $\text{Mn}_3\text{O}_4$  NR/reduced graphene oxide paper ( $\text{Mn}_3\text{O}_4$  NR/rGO paper) has an out-of-plane porous structures through reduction process, leading to facile lithium transfer without loss. The porous  $\text{Mn}_3\text{O}_4$  NR/rGO paper (p $\text{Mn}_3\text{O}_4$  NR/rGO) shows the first discharge and charge capacities of 943 and 627  $\text{mA}\cdot\text{h}\cdot\text{g}^{-1}$ , respectively and Coulombic efficiency of 66.5%. The irreversible capacity loss is related to the formation of the solid electrolyte interphase (SEI) layer and electrolyte decomposition. After 100 cycles, the p $\text{Mn}_3\text{O}_4$  NR/rGO paper compared to an rGO paper maintains a high specific capacity of 573  $\text{mA}\cdot\text{h}\cdot\text{g}^{-1}$ , indicating that the p $\text{Mn}_3\text{O}_4$  NR and rGO contribute substantially to the capacity retention. The p $\text{Mn}_3\text{O}_4$  NR/rGO at various current densities, 50, 100, 500, 1000,

and 2000 mA g<sup>-1</sup>, delivers a high capacity of 692, 618, 411, 313, and 196 mA h g<sup>-1</sup>, respectively.

Secondly, GO is treated by acid, HNO<sub>3</sub>, in order to make in-plane pores on the graphene surface. The acid-treated reduced graphene oxide (ArGO) provides Li ion transport pathway through pores and electron transport pathway over the entire graphene surface. Mn<sub>3</sub>O<sub>4</sub> NR, which is a one-dimensional (1D) nanomaterial, akin to ArGO has a large surface area and provides efficient 1D electron transport and short Li ion diffusion distance to be capable of improving the electrochemical performance in LIBs. The acid-treated reduced graphene oxide/Mn<sub>3</sub>O<sub>4</sub> nanorod (ArGO/Mn<sub>3</sub>O<sub>4</sub> NR) is simply prepared by mixing acid-treated graphene oxides (AGO) with MnOOH nanorods (MnOOH NRs) and reduction. The ArGO/Mn<sub>3</sub>O<sub>4</sub> NR electrode exhibits the first discharge and charge capacities of 1130 and 778 mA·h·g<sup>-1</sup> at 200 mA·g<sup>-1</sup>, respectively and a low initial irreversible capacity of 32%. Coulombic efficiency is recovered to 98% after 3 cycles. After 100 cycles, the overall capacity reaches to 749 mA·h·g<sup>-1</sup>.

Lastly, SnO<sub>2</sub> nanoparticles are hydrothermally synthesized onto the graphene surface. In this study, graphite is oxidized and then activated by nitric acid in order to introduce in-plane pores into graphite oxide.

After reduction, an ArGO is used as a host material and buffer layer for SnO<sub>2</sub> to avoid suffering from pulverization while Li ion is inserted into and extracted from SnO<sub>2</sub>. Additionally, Li ion diffusion and electron transfer can go through or on ArGO resulting in enhancing the rate capability of the electrode. The ArGO/SnO<sub>2</sub> (AGS) electrode displays the first charge and discharge capacity of 979 and 2030 mA h g<sup>-1</sup>. The Coulombic efficiency of the AGS electrode corresponds to 48% with respect to the first cycle. Moreover, the AGS electrode maintains 720 and 569 mA h g<sup>-1</sup> at 200 and 500 mA g<sup>-1</sup> without considerable capacity loss when it reaches 200 cycles.

The research implies that such graphene-based nanocomposites enable electrode materials to achieve high capacity, high rate capability and stable cyclability in LIBs. Therefore, it is expected that these nanomaterials have a great potential to sufficiently surpass the performance of existing LIBs.

**Keywords:** Graphene, One-dimensional material, Manganese oxide, Tin oxide, Manganite, Nanocomposites, Lithium ion batteries.

**Student Number:** 2012-22448

# Contents

<b>Chapter 1. Introduction</b> .....	24
<b>Chapter 2. Literature survey</b> .....	31
2.1. Lithium ion batteries .....	32
2.2. Graphene-based nanomaterials as anodes for lithium ion batteries .....	43
2.2.1. Graphene and graphene oxide .....	43
2.2.2. Graphene paper as an electrode .....	48
2.2.3. Graphene/metal oxide as an electrode .....	56
2.3. Challenges to problems.....	63
2.3.1. Graphene/metal oxide as an electrode .....	63
2.3.2. Improvement of lithium ion and electron transport for rate capability .....	65
<b>Chapter 3. Experiments</b> .....	69
3.1. Materials.....	70
3.2. Synthesis of graphene oxides and acid-treated graphene oxides .....	70
3.3. Synthesis of MnOOH nanorods .....	71
3.4. Fabrication of pMn <sub>3</sub> O <sub>4</sub> NR/rGO paper .....	72

3.5. Fabrication of Mn <sub>3</sub> O <sub>4</sub> NR, rGO/Mn <sub>3</sub> O <sub>4</sub> NR and ArGO/Mn <sub>3</sub> O <sub>4</sub> NR.....	72
3.6. Synthesis of SnO <sub>2</sub> , rGO/SnO <sub>2</sub> and ArGO/SnO <sub>2</sub> .....	73
3.7. Material characteriazation.....	74
3.8. Electrochemical measurements.....	74
<b>Chapter 4. Results and Discussion .....</b>	<b>77</b>
4.1. Porous Mn <sub>3</sub> O <sub>4</sub> Nanorod/Reduced Graphene Oxide Hybrid Paper as a Flexible and Binder-free Anode Material for Lithium Ion Battery.....	78
4.2. An Acid-treated Reduced Graphene Oxide/Mn <sub>3</sub> O <sub>4</sub> Nanorod Nanocomposite as an Enhanced Anode Material for Lithium Ion Batteries .....	96
4.3. An Acid-treated Reduced Graphene Oxide/Tin Oxide Nanocomposite as an Anode Material for Lithium Ion Batteries .....	114
<b>Chapter 5. Conclusion.....</b>	<b>127</b>
<b>References .....</b>	<b>131</b>

**Bibliography** .....144

**국문 초록 (Abstract in Korean)** .....150

## **List of Figures**

<b>Figure 1</b>	Schematic of a LIB. (from Ref. 62. B. Dunn et al., Science, 2011, 334, 928.).....	37
<b>Figure 2</b>	Gravimetric power and energy densities for different rechargeable batteries. (from Ref. 61. B. Dunn et al., Science, 2011, 334, 928.).....	38
<b>Figure 3</b>	Fully electrical cars, such as the Tesla roadster (bottom left) and the latest mobile phones (bottom right) (from Ref. 4. M. Armand et al., Nature, 2008, 451, 652.).....	39
<b>Figure 4</b>	Battery chemistry over the years. (from Ref. 4. M. Armand et al., Nature, 2008, 451, 652.) .....	40
<b>Figure 5</b>	Schematic of the preparation of graphene/metal oxide composites with synergistic effects between graphene and metal oxides. (from Ref. 8. Z. S. Wu et al., Nano Energy, 2012, 1, 107.).....	41
<b>Figure 6</b>	Schematic illustration of synthetic methods of 3D	

	graphene based composites. (from Ref. 11. B. Luo et al., Energy Environ. Sci., 2015, 8, 456) .....	42
<b>Figure 7</b>	Chemical structure of graphite oxide. (from Ref. 13. S. Park et al., Nat. Nanotechnol., 2009, 4, 217.).....	45
<b>Figure 8</b>	Several methods of mass-production of graphene (from Ref. 15. K. S. Novoselov et al., Nature, 2012, 490, 192.)..	46
<b>Figure 9</b>	Digital camera images of graphene oxide paper. (from Ref. 23. D. A. Dikin et al., Nature 2007, 448, 457.).....	50
<b>Figure 10</b>	Photograph of two pieces of free-standing graphene paper fabricated by vacuum filtration of chemically prepared graphene dispersions. (from Ref. 25. H. Chen et al., Adv. Mater. 2008, 20, 3557.).....	51
<b>Figure 11</b>	SEM image of graphene paper. (from Ref. 26. C. Wang et al., Chem. Mater., 2009, 21, 2604.) .....	52

**Figure 12** Schematic diagram for the fabrication of graphene paper through vacuum assisted filtration. (from Ref. 27. Y. Hu et al., *Electrochim. Acta*, 2013, 91, 227.) .....53

**Figure 13** SEM images of graphene papers: (a–c) cross sections of 1.5, 3 and 10  $\mu\text{m}$  graphene paper, respectively; (d) top view of 10  $\mu\text{m}$  graphene paper. (from Ref. 27. Y. Hu et al., *Electrochim. Acta*, 2013, 91, 227.) .....54

**Figure 14** SEM images of graphene paper showing the (A) undulating paper surface and (B) local heterogeneities along a fractured edge. (from Ref. 28. A. Abouimrane et al., *J. Phys. Chem. C*, 2010, 114, 12800.).....55

**Figure 15** Schematic of structural models of graphene/metal oxide composites: (a) Anchored model: nanosized oxide particles are anchored on the surface of graphene. (b) Wrapped model: metal oxide particles are wrapped by graphene. (c) Encapsulated model: oxide particles are encapsulated by graphene. (d) Sandwich-like model:

graphene serves as a template for the creation of a metal oxide/graphene/metal oxide sandwich-like structure. (e) Layered model: a structure composed of alternating layers of metal oxide nanoparticles and graphene. (f) Mixed model: graphene and metal oxide particles are mechanically mixed and graphene forms a conductive network among the metal oxide particles. Red: metal oxide particles; Blue: graphene sheets. (from Ref. 8. Z. S. Wu et al., Nano Energy, 2012, 1, 107.).....62

**Figure 16** Schematic illustrations showing restacking of graphene oxide and graphene. (from Ref. 70. J. H. Lee et al., ACS Nano, 2013, 7, 9366.) .....64

**Figure 17** Schematic drawing of the introduction of in-plane pores into chemically exfoliated graphene oxide and the subsequent filtration into a holey graphene oxide paper. (from Ref. 71. X. Zhao et al., ACS Nano, 5, 8739.) .....66

**Figure 18** The evolution of nanopores; (a–d) scale bar = 2 um and

(e–h) scale bar = 1 um. (from Ref. 70. X. Wang et al., Sci. Rep., 2013, 3. 1996.).....	67
<b>Figure 19</b> Conceptual illustrations of lithium ion diffusion pathways in (a) G/LFP and (b) CA-G/LFP. (from Ref. 73. J. Ha et al., Nanoscale, 2013, 5, 8647.) .....	68
<b>Figure 20</b> Schematic illustration of the synthesis of pMn <sub>3</sub> O <sub>4</sub> NR/rGO paper .....	82
<b>Figure 21</b> Cross-sectional SEM images of GO paper (a), MnOOH NR/GO paper (b) and pMn <sub>3</sub> O <sub>4</sub> NR/rGO paper (c and d)...	83
<b>Figure 22</b> Top-view SEM images of GO paper (a), MnOOH NR/GO paper (b) and pMn <sub>3</sub> O <sub>4</sub> NR/rGO paper (c and d) .....	84
<b>Figure 23</b> TEM and HRTEM Images of MnOOH NR/GO paper (a and d) and pMn <sub>3</sub> O <sub>4</sub> NR/rGO paper (b, c, and e). (f) Dark-field TEM image and the corresponding Mn, C, and O element mapping.....	85

<b>Figure 24</b>	(a) XRD patterns of GO and rGO and (b) MnOOH NR/GO paper and pMn <sub>3</sub> O <sub>4</sub> NR/rGO paper .....	92
<b>Figure 25</b>	(a) FT-IR transmittance spectra of pMn <sub>3</sub> O <sub>4</sub> NR/rGO and MnOOH NR/GO paper and (b) TGA curve of pMn <sub>3</sub> O <sub>4</sub> NR/rGO paper.....	93
<b>Figure 26</b>	(a) Cyclic voltammograms of pMn <sub>3</sub> O <sub>4</sub> NR/rGO paper at a scanning rate of 0.1 mV s <sup>-1</sup> , (b) charge–discharge profiles of pMn <sub>3</sub> O <sub>4</sub> NR/rGO paper, (c) comparative cycle performance of papers at a current density of 100 mA g <sup>-1</sup> and (d) rate capability of pMn <sub>3</sub> O <sub>4</sub> NR/rGO and bare rGO paper at various current densities .....	94
<b>Figure 27</b>	(a) MnOOH nanorods and (b) Mn <sub>3</sub> O <sub>4</sub> nanorods after the thermal treatment.....	95
<b>Figure 28</b>	Schematic preparation of nanocomposite.....	99
<b>Figure 29</b>	XRD patterns of (a) MnOOH NR, (b) Mn <sub>3</sub> O <sub>4</sub> NR, (c)	

	rGO/Mn <sub>3</sub> O <sub>4</sub> and (d) ArGO/Mn <sub>3</sub> O <sub>4</sub> .....	100
<b>Figure 30</b>	(a) Nitrogen adsorption/desorption isotherms and (b) pore-size distribution of Mn <sub>3</sub> O <sub>4</sub> NR, rGO/Mn <sub>3</sub> O <sub>4</sub> and ArGO/Mn <sub>3</sub> O <sub>4</sub> .....	101
<b>Figure 31</b>	SEM images of (a) MnOOH, (b) Mn <sub>3</sub> O <sub>4</sub> , (c, d) rGO/Mn <sub>3</sub> O <sub>4</sub> and (e, f) ArGO/Mn <sub>3</sub> O <sub>4</sub> NR .....	102
<b>Figure 32</b>	SEM images of the ArGO/Mn <sub>3</sub> O <sub>4</sub> NR after 100 cycles....	103
<b>Figure 33</b>	TEM and HR-TEM images of (a, b) rGO/Mn <sub>3</sub> O <sub>4</sub> and (c, d) ArGO/Mn <sub>3</sub> O <sub>4</sub> NR .....	109
<b>Figure 34</b>	Cyclic voltammograms and charge–discharge profiles of (a, b) Mn <sub>3</sub> O <sub>4</sub> , (c, d) rGO/Mn <sub>3</sub> O <sub>4</sub> and (e, f) ArGO/Mn <sub>3</sub> O <sub>4</sub> NR.....	110
<b>Figure 35</b>	Comparative cycle performance of Mn <sub>3</sub> O <sub>4</sub> NR, rGO/Mn <sub>3</sub> O <sub>4</sub> NR and ArGO/Mn <sub>3</sub> O <sub>4</sub> NR at a current density	

of 200 mA g <sup>-1</sup> and rate capability of Mn <sub>3</sub> O <sub>4</sub> NR, rGO/Mn <sub>3</sub> O <sub>4</sub> NR and ArGO/Mn <sub>3</sub> O <sub>4</sub> NR at various current densities .....	111
<b>Figure 36</b> Cycle performance of ArGO at a current density of 200 mA g <sup>-1</sup> .....	112
<b>Figure 37</b> Comparative cycle performance of Mn <sub>3</sub> O <sub>4</sub> NR, rGO/Mn <sub>3</sub> O <sub>4</sub> NR and ArGO/Mn <sub>3</sub> O <sub>4</sub> NR.....	113
<b>Figure 38</b> Schematic diagram for preparation of the nanocomposite .....	116
<b>Figure 39</b> X-ray diffraction patterns of SnO <sub>2</sub> , GS and AGS (a, b and c).....	117
<b>Figure 40</b> SEM images of AGS (a) and GS (b).....	118
<b>Figure 41</b> TEM images of ArGO (a), SnO <sub>2</sub> (b), GS (c) and AGS (d) .....	119

**Figure 42** HRTEM images of GS (a and b) and AGS (c and d).....120

**Figure 43** Dark-field TEM image and the corresponding Sn, C, and O element mapping.....121

**Figure 44** Galvanostatic charge–discharge profiles of SnO<sub>2</sub>, GS and AGS at 200 mA g<sup>-1</sup> (a, b and c), respectively. Cyclic voltammetry curves of SnO<sub>2</sub>, GS and AGS (d, e and f) ...125

**Figure 45** Cycling performance at 200 mA g<sup>-1</sup> and 500 mA g<sup>-1</sup> (a and b) and rate performances of SnO<sub>2</sub>, GS and AGS at different current densities .....126

## **List of Tables**

<b>Table 1</b>	Properties of graphene obtained by different methods .....	47
<b>Table 2</b>	The pros and cons of graphene, metal oxides, and graphene/metal oxide composites in LIBs.....	61

# **Chapter 1. Introduction**

## 1. Introduction

Rechargeable Li-ion batteries (LIBs) for clean and sustainable energy storages are considered as the most promising power source, from portable electronics to electric vehicles, due to the increasing concerns about limited energy supplies [1, 2]. Despite the fact that LIBs have attracted great concerns due to high power density ( $150 \text{ Wh kg}^{-1}$ ) and high energy density ( $400 \text{ Wh L}^{-1}$ ), the dominant graphite anode material is not able to meet the customers' ever increasing requirements with its limited specific capacity ( $372 \text{ mA h g}^{-1}$ ) and poor rate capability [3-5]. Accordingly, a lot of research effort has been focused on searching for advanced anode materials with high capacity, good rate capability and long cycle life to meet the growing demand for LIBs with higher energy and power densities [6-8].

Many transition metal oxides like  $\text{Fe}_x\text{O}_y$ ,  $\text{Co}_3\text{O}_4$ ,  $\text{Mn}_x\text{O}_y$ ,  $\text{SnO}_2$  and  $\text{TiO}_2$  have emerged as anode materials for LIBs owing to their high specific capacities [9-16]. Among these metal oxides,  $\text{Mn}_3\text{O}_4$  is a promising anode material because of its high theoretical capacity ( $937 \text{ mA h g}^{-1}$ ) which is almost three times as high as that of graphite, low price, natural abundance, low discharge potential and low toxicity [17, 18]. In addition, one dimensional (1D) nanomaterials not only has a

large surface-to-volume ratio but also provides efficient 1D electron transport pathway and short Li ion diffusion length, which can improve the electrochemical performance in LIBs [19, 20]. Nevertheless, its practical application to LIBs is limited due to its poor electrical conductivity ( $\sim 10^{-7}$ - $10^{-8}$  S cm<sup>-1</sup>), pulverization, unstable solid electrolyte interface (SEI) formation and severe volume expansion in the Li<sup>+</sup> insertion/extraction process, which lead to a large reversible capacity loss, poor cycling, and poor rate performance [21-25]. SnO<sub>2</sub> is another promising anode material for LIBs due to high specific capacity (782 mAh g<sup>-1</sup>) compared to graphite, low operation potential and high abundance [26-37]. In spite of these advantages, the inherent poor conductivity and large volume expansion/contraction (>200%) during cycling have hampered its practical application in LIBs [38-44]. To overcome these limitations, many researches have been attempted in order to fabricate various nanostructures of Mn<sub>3</sub>O<sub>4</sub> and SnO<sub>2</sub> with conductive carbon materials, such as graphene and CNT, to improve the electrical conductivity and structural stability [17, 22, 45-51].

Carbon materials, such as amorphous carbon, carbon nanofibers and carbon nanotubes, have proved to be a useful strategy to improve the

cycling stability and the overall capacity of the transition metal oxides in LIBs because of their unique buffering ability. In particular, graphene, which is a two-dimensional and one-atom-thick carbon material, has been considered as an ideal host material to anchor transition metal oxides owing to high conductivity, excellent mechanical properties and high surface area [52, 53]. Therefore, graphene/metal oxide nanocomposites have been investigated as good candidates for anode materials in LIBs. Furthermore, introduction of in-plane pores on graphene provides a high density of cross-plane  $\text{Li}^+$  diffusion channels, so that reduced graphene oxides by acid treatment is expected to exhibit the excellent electrochemical performance [54, 55].

In the previous reports, the nanocomposites of  $\text{Mn}_3\text{O}_4$  and  $\text{SnO}_2$  with graphene exhibited excellent electrochemical performance. For example, Wang et al. synthesized a  $\text{Mn}_3\text{O}_4$ /graphene hybrid via a two-step, solution-phase method, and obtained a high reversible capacity of  $810 \text{ mA h g}^{-1}$  at a current density of  $40 \text{ mA g}^{-1}$  [17]. Ding et al. reported that  $\text{Mn}_3\text{O}_4$ /graphene showed a capacity of  $500 \text{ mA h g}^{-1}$  at  $60 \text{ mA g}^{-1}$  after 100 cycles [56]. The rGO/ $\text{Mn}_3\text{O}_4$  electrode reported by Zhao et al. delivered a reversible capacity of  $1294 \text{ mA h g}^{-1}$  at 100

mA g<sup>-1</sup> after 100 cycles [57]. Yoo et al. reported synthesis of 2 nm SnO<sub>2</sub> particles that are sandwiched between reduced graphene oxide and carbon by stirring Sn<sup>4+</sup>/GO/ascorbic acid at low temperature [58]. Yang et al. described microwave assisted hydrothermal synthesis of 7.5 nm SnO<sub>2</sub> particles on reduced graphene oxide [59]. Wang et al. applied CNT to a SnO<sub>2</sub>/graphene composite to reinforce the structure of aerogel composite and explained that this structure showed excellent cycle stability and rate capability [60].

This doctoral dissertation includes three theses which are ‘Porous Mn<sub>3</sub>O<sub>4</sub> Nanorod/Reduced Graphene Oxide Hybrid Paper as a Flexible and Binder-free Anode Material for Lithium Ion Battery’, ‘An Acid-treated Reduced Graphene Oxide/Mn<sub>3</sub>O<sub>4</sub> Nanorod Nanocomposite as an Enhanced Anode Material for Lithium Ion Batteries’ and ‘An Acid-treated Reduced Graphene Oxide/Tin Oxide Nanocomposite as an Anode Material for Lithium Ion Batteries’. The first thesis demonstrates the preparation of porous manganese oxide nanorod/reduced graphene oxide (pMn<sub>3</sub>O<sub>4</sub> NR/rGO) paper, as a flexible and binder-free anode material, by simple filtration combined with a thermal treatment. In the hybrid paper, pMn<sub>3</sub>O<sub>4</sub> NRs with large aspect ratios are distributed on rGO homogeneously. These unique

structures are beneficial to improving electrochemical performance owing to the large surface area and void space to buffer volume expansion. Furthermore, pMn<sub>3</sub>O<sub>4</sub> NR can act as a physical buffer to expand the interlayer spacing of rGO sheets, resulting in the formation of many new pores between the nanorods and rGO sheets to afford open channels and pathways for Li ion transport. As a consequence, the pMn<sub>3</sub>O<sub>4</sub> NR/rGO paper exhibits a high reversible capacity and cycling stability. Porous manganese oxide nanorod/reduced graphene oxide paper is expected to play a crucial role in flexible energy storage devices. The second thesis demonstrates the preparation of ArGO/Mn<sub>3</sub>O<sub>4</sub> nanocomposites by simple mixing and thermal treatment. Mn<sub>3</sub>O<sub>4</sub> NRs in the nanocomposites has a high aspect ratio and is homogeneously distributed between ArGO. This structure is effective to improve electrochemical performance due to the presence of various new pores between Mn<sub>3</sub>O<sub>4</sub> NR and ArGO to provide open channels and pathways for Li ions. As a consequence, ArGO/Mn<sub>3</sub>O<sub>4</sub> nanocomposites exhibits a high reversible capacity and cycling stability. The ArGO/Mn<sub>3</sub>O<sub>4</sub> nanocomposites is expected to present obviously improved electrochemical properties compared with bare oxides and reduced graphene oxide-wrapped manganese oxide

nanorods. In the last thesis, graphene was oxidized and then activated by  $\text{HNO}_3$  in order to introduce in-plane pores into graphene. These acid-treated reduced graphene oxides were used as buffer layers for  $\text{SnO}_2$  to alleviate suffering from pulverization, which is caused by Li ion insertion/extraction during cycling, and enhance electron transfer over graphene. Additionally, they could help Li ions facilitate diffusion through graphene so that the rate capability of electrodes was expected to be much better performed than bare electrodes.

## **Chapter 2. Literature survey**

## 2. Literature survey

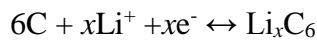
### 2.1. Lithium ion batteries

Unlike the primary battery, LIBs can be recharged, therefore, have been considered as the most promising energy storage system for a wide variety of applications. LIBs have revolutionized portable electronic devices including cellular phones, laptops, drones and digital cameras [4, 8, 61-63]. They are also important power sources for future electric vehicles, hybrid electric vehicles and emerging smart grids [64, 65]. Rechargeable LIBs offer energy densities 2-3 times and power densities 5-6 times higher than conventional batteries (**Figure 1**): such as Ni–MH, Ni–Cd, and Pb acid batteries [6, 66]. Rechargeable LIBs have many other advantages such as stable cyclability, low self-discharge, high operating voltage, wide temperature window, and no memory effect.

The LIBs don't contain lithium metal but lithium ion. It is usually comprised of  $\text{LiCoO}_2$  as cathode, carbon as anode and organic electrolyte of lithium hexafluorophosphate ( $\text{LiPF}_6$ ) salt with ethylene carbonate-organic solvent mixture [67-69]. The fundamental physics and chemistry of the rechargeable LIB are based on a process known as intercalation/deintercalation or insertion/extraction; the reversible

insertion of guest atoms (like lithium) into solid hosts (the battery electrode materials). The electrochemical reactions at an anode and a cathode during the charge/discharge are the following (**Figure 2**):

Anode:



Cathode:



A battery is a device that converts the chemical energy of active materials contained in the cell into electrical energy by an electrochemical oxidation/reduction reaction. In the true sense, the term, battery, refers to a collection of two or more electrochemical cells, but is also commonly used in single cells. The cell is made of a special internal structure so that the electrochemical reaction takes place instead of the chemical reaction and the electrons can escape to the outside through the conductor. The electron flow flowing through the conductor provides a useful work for the human being as a source of electric energy.

Techniques and approaches for providing new properties while complementing the properties of independent and individual materials such as organic/inorganic mixed composite and hybrid materials have been applied in various fields for a long time. In order to increase the energy density of next-generation high-capacity and energy-source devices such as LIBs and metal-air batteries, which have been attracting much attention as energy storage devices in the recent past, electrode material performance must be secured first. Particularly, a conventional carbon material such as graphite, which is essentially used for imparting electronic conductivity to an electrode material serving as an energy storage, has been studied to be replaced with a functionalized carbon compound such as graphene or carbon nanotube [70, 71].

In 1991, Sony Corporation of Japan commercialized 3V lithium ion rechargeable batteries, which are three times higher in operating voltage than Ni-MH batteries. LIBs can be made smaller and lighter due to the emergence of LIBs with improved energy density (**Figure 3**), leading to the market of portable devices such as mobile phones and notebooks [2, 72]. Currently, applications of LIBs are not only electric power for portable devices but electric bicycles and electric

tools as well as transportation applications such as HEV, PHEV, EV, etc. and smart grid applied power storage [3]. In the future, large-sized secondary battery market such as electric vehicle is demanding high capacity and high output technology of lithium ion battery (**Figure 4**).

Due to its excellent electrical and thermal properties, Graphene is expected to be a candidate material for various fields, such as transparent electrodes, heat dissipation materials, sensors, energy storage and environment, and graphene materials suitable for each application have been developed [73, 74]. In addition, metal oxides exhibiting electrochemical activation with lithium ions have been studied mainly in transition metal oxide series. It is also important to understand the properties of the two individual materials in graphene/metal oxide composites (**Figure 5**). It is generally known that a composite material with a carbon compound such as graphene is advantageous for imparting partial conductivity to a metal oxide having a relatively low electrical conductivity [35, 75].

Nanomaterials, which are classified in zero-dimensional (0D) as nanospheres, one-dimensional (1D) as nanowires, two-dimensional (2D) as nanosheets or nanoplates, and three-dimensional (3D), offer many advantages such as high surface area, novel size effects,

significantly enhanced kinetics and so on in energy storage applications (**Figure 6**). The smaller size of the nanomaterial not only reduces dimensional changes due to chemical reactions and phase transitions but can also provide better charge transfer, mass and heat [76, 77].

In this chapter, I would like to introduce classification and preparation of graphene-based nanomaterials for electrode in LIBs. In following section, LIBs and anode materials as LIBs are introduced and described. And then the theses are overviewed.

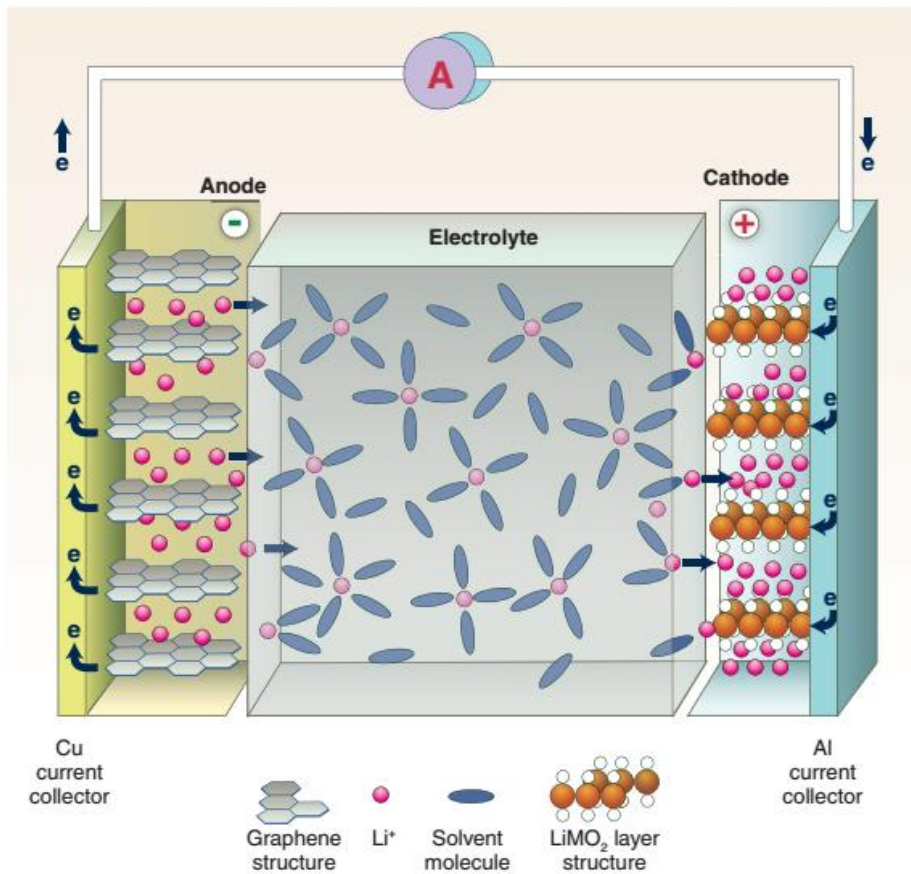


**Figure 1** Schematic of a LIBs. (from Ref. 6. B. Dunn et al., *Science*, 2011, 334, 928.)

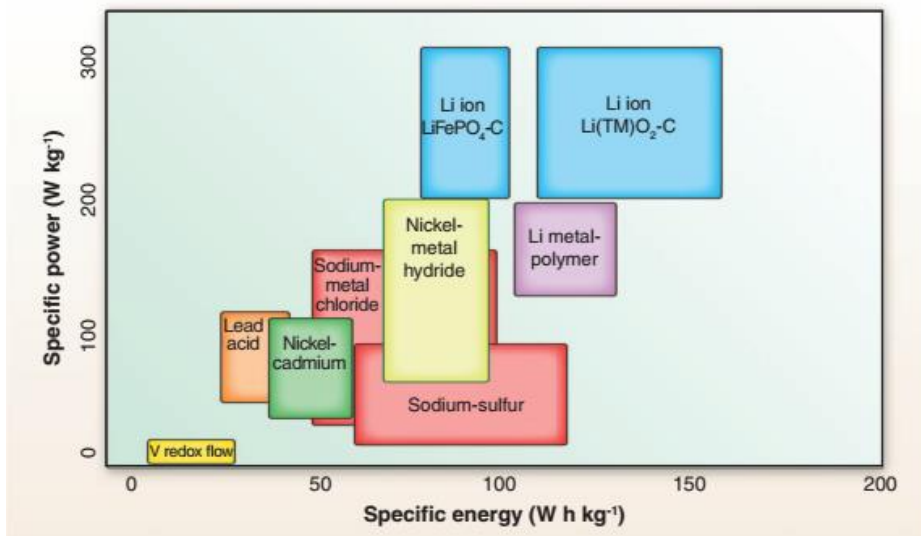


**Figure 2** Gravimetric power and energy densities for different rechargeable batteries. (from Ref. 6. B. Dunn et al., *Science*, 2011, 334, 928.)

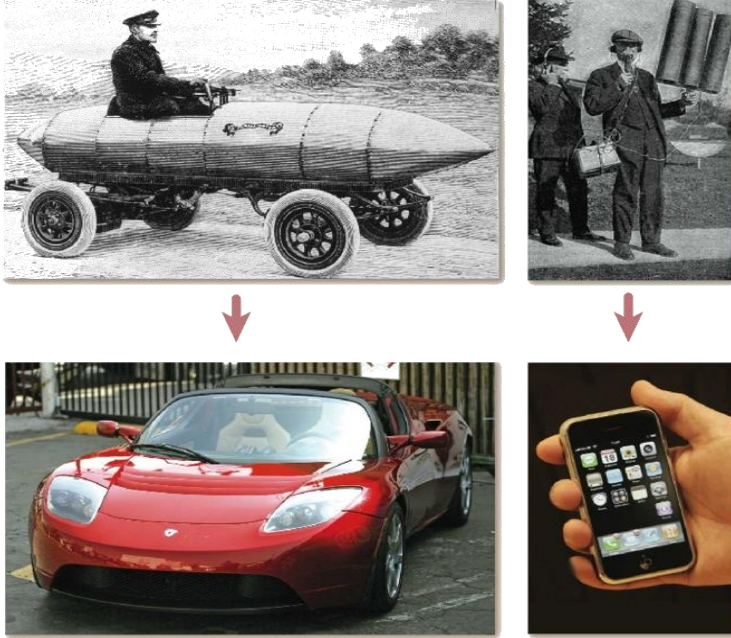


**Figure 3** Fully electrical cars, such as the Tesla roadster (bottom left) and the latest mobile phones (bottom right) (from Ref. 2. M. Armand et al., *Nature*, 2008, 451, 652.)

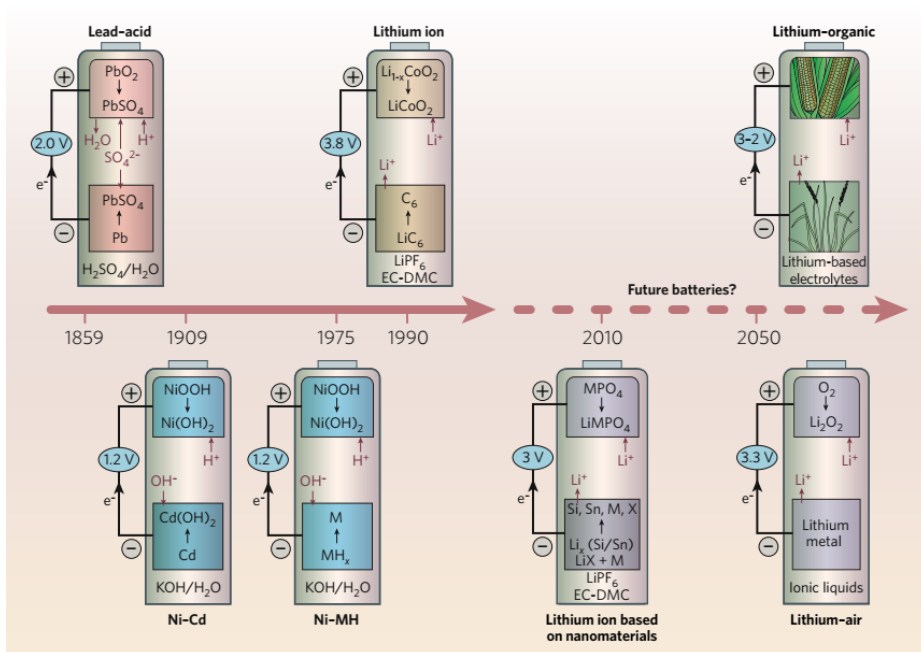


**Figure 4** Battery chemistry over the years. (from Ref. 2. M. Armand et al., *Nature*, 2008, 451, 652.)

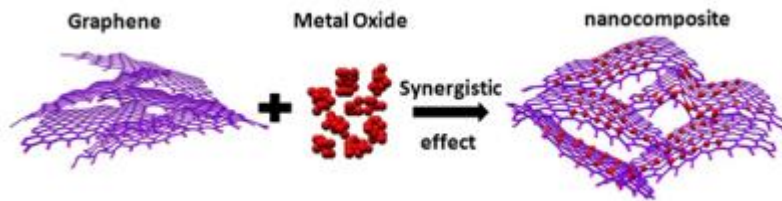


**Figure 5** Schematic of the preparation of graphene/metal oxide composites with synergistic effects between graphene and metal oxides. (from Ref. 35. Z. S. Wu et al., *Nano Energy*, 2012, 1, 107.)

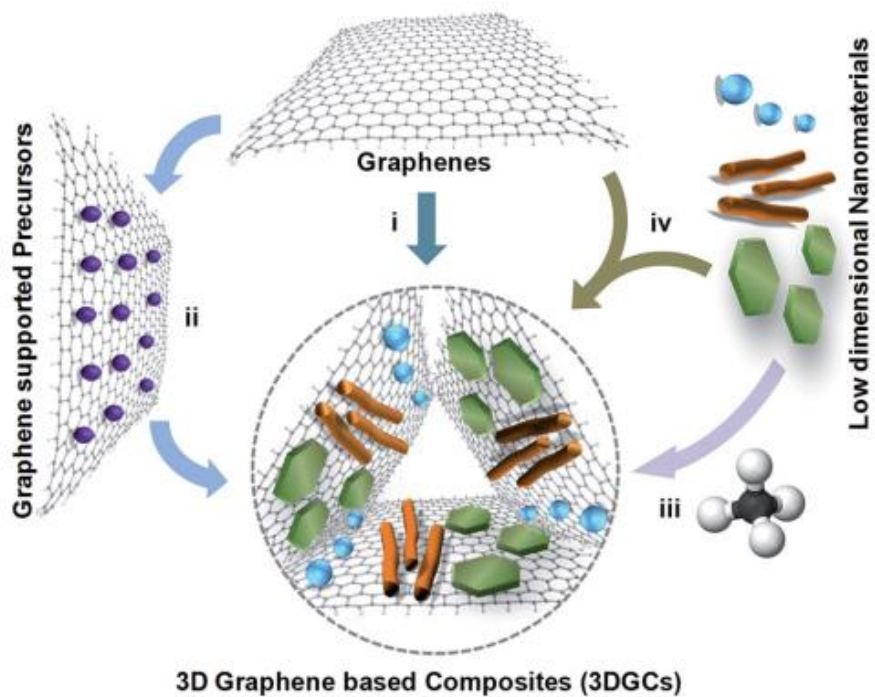


**Figure 6** Schematic illustration of synthetic methods of 3D graphene based composites. (from Ref. 77. B. Luo et al., *Energy Environ. Sci.*, 2015, 8, 456)

## 2.2 Graphene-based nanomaterials as anodes for lithium ion batteries

### 2.2.1. Graphene and graphene oxide

Graphene has recently emerged as an alternative energy storage material with excellent properties, such as low weight, chemically inert, low price and so on. Graphene is a large monolayer sheet of sp<sup>2</sup>-bonded carbon, which has unique optical, electrical, mechanical and electrochemical properties. The surface area of graphene is about 2630 m<sup>2</sup> g<sup>-1</sup>, which is hugely favorable for energy storage applications. Graphene is conductive and easy to functionalize with other molecules [78]. The most important graphene by being chemically derived, is graphene oxide (GO) [79, 80], which is usually prepared from graphite by oxidization to graphite oxide and consequent exfoliation to GO (**Figure 7**). Graphene can be fabricated by various methods [81]: (a) the typical method of thermal decomposition of graphite oxide and the following reduction of GO to graphene [82], resulting in few and multilayer graphene structures [83]; (b) chemical vapour deposition (CVD) growth by use of a metal catalyst [84]; (c) the conventional method of mechanical cleavage of graphite [85]; (d) unzipping carbon nanotubes [86, 87]; and (e) electrochemical

exfoliation of graphite [88] (**Figure 8**). The comparison of above methods for fabrication of graphene is summarized in **Table 1**.

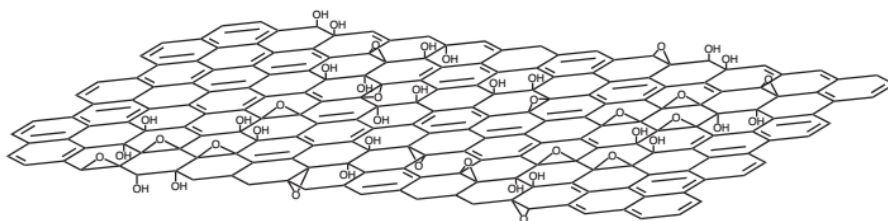


**Figure 7** Chemical structure of graphite oxide. (from Ref. 79. S. Park et al., *Nat. Nanotechnol.*, 2009, 4, 217.)

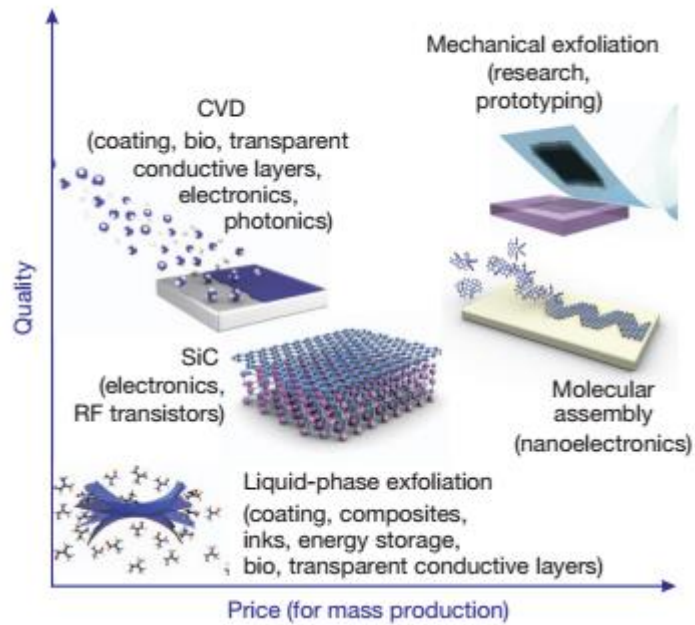


**Figure 8** Several methods of mass-production of graphene (from Ref. 81. K. S. Novoselov et al., *Nature*, 2012, 490, 192.)

Method	Crystallite size ( $\mu\text{m}$ )	Sample size (mm)	Charge carrier mobility (at ambient temperature) ( $\text{cm}^2\text{V}^{-1}\text{s}^{-1}$ )	Applications
Mechanical exfoliation	>1,000	>1	$>2 \times 10^5$ and $> 10^6$ (at low temperature)	Research
Chemical exfoliation	$\leq 0.1$	Infinite as a layer of overlapping flakes	100 (for a layer of overlapping flakes)	Coatings, paint/ink, composites, transparent conductive layers, energy storage, bioapplications
Chemical exfoliation via graphene oxide	$\sim 100$	Infinite as a layer of overlapping flakes	1 (for a layer of overlapping flakes)	Coatings, paint/ink, composites, transparent conductive layers, energy storage, bioapplications
CVD	1,000	$\sim 1,000$	10,000	Photonics, nanoelectronics, transparent conductive layers, sensors, bioapplications
SiC	50	100	10,000	High-frequency transistors and other electronic devices

**Table 1** Properties of graphene obtained by different methods. (from Ref. 81. K. S. Novoselov et al., *Nature*, 2012, 490, 192.)

### 2.2.2. Graphene paper as an electrode

GO sheets dispersed in water can be assembled into a well-ordered structure under a directional flow like vacuum filtration process, yielding flexible and sturdy GO paper [89]. GO paper is more superb than many other analogues in stiffness and strength, however, a lack of electrical conductivity constrains its use (**Figure 9**). Although GO paper can be reduced to graphene, called reduced graphene oxide (rGO), by thermal treatment, the structure and mechanical properties significantly deteriorate after thermal annealing. Graphene can be also dispersed by carefully controlled reduction of GO dispersions with hydrazine [90, 91]. Graphene paper is then fabricated by filtration of a measured amount of graphene dispersion through an Anodisc membrane filter, followed by air drying and peeling from the filter (**Figure 10**).

Flexible and robust graphene paper (**Figure 11**) may be adopted to an electrode in energy storage devices [92]. Accordingly, the electrochemical properties of graphene paper electrodes used in LIBs can be measured. The papers can be readily fabricated using assembly method (**Figure 12**) under a directional flow [93]. The introduction of freestanding graphene paper into lithium ion battery assembly offers

several advantages (**Figure 13**). Such a design generally requires fewer steps in anode fabrication and battery assembly, with potential to eliminate electric conductors and polymer binders that are used in conventional powder-based anodes fabrication [94]. Graphene paper possesses equal or even higher flexibility than that of metal foils do but has much lower mass, which renders the fabrication of thin film battery possible (**Figure 14**). Research on graphene paper as anodes for LIBs is developing very rapidly [95, 96].

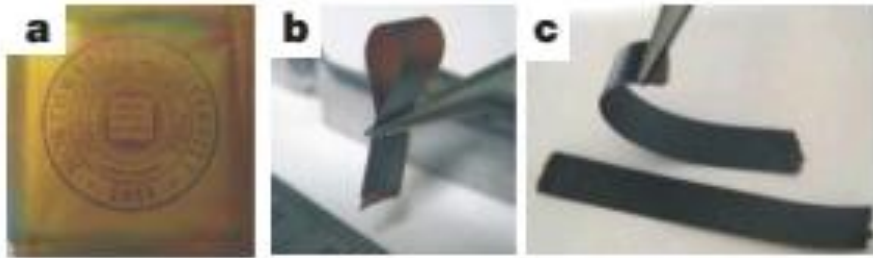


**Figure 9** Digital camera images of graphene oxide paper. (from Ref. 89. D. A. Dikin et al., *Nature*, 2007, 448, 457.)

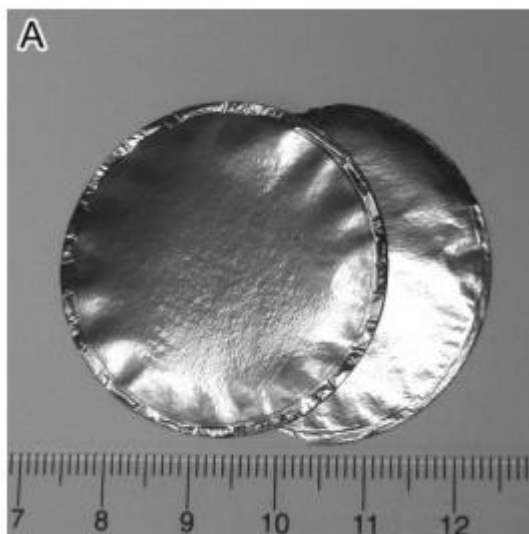


**Figure 10** Photograph of two pieces of free-standing graphene paper fabricated by vacuum filtration of chemically prepared graphene dispersions. (from Ref. 91. H. Chen et al., *Adv. Mater.*, 2008, 20, 3557.)

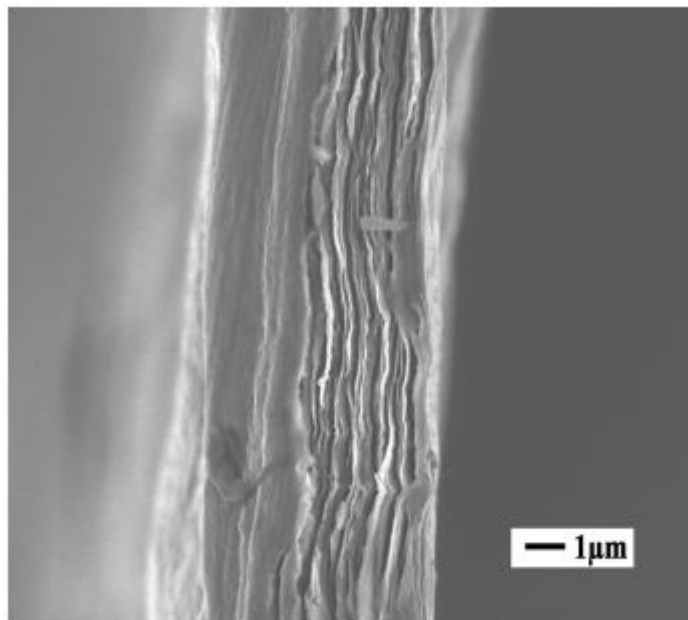


**Figure 11** SEM image of graphene paper. (from Ref. 92. C. Wang et al., *Chem. Mater.*, 2009, 21, 2604.)

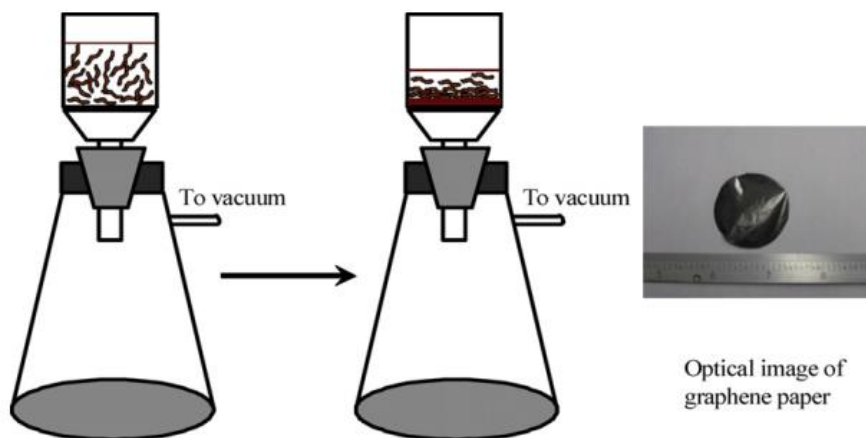


**Figure 12** Schematic diagram for the fabrication of graphene paper through vacuum assisted filtration. (from Ref. 93. Y. Hu et al., *Electrochim. Acta*, 2013, 91, 227.)

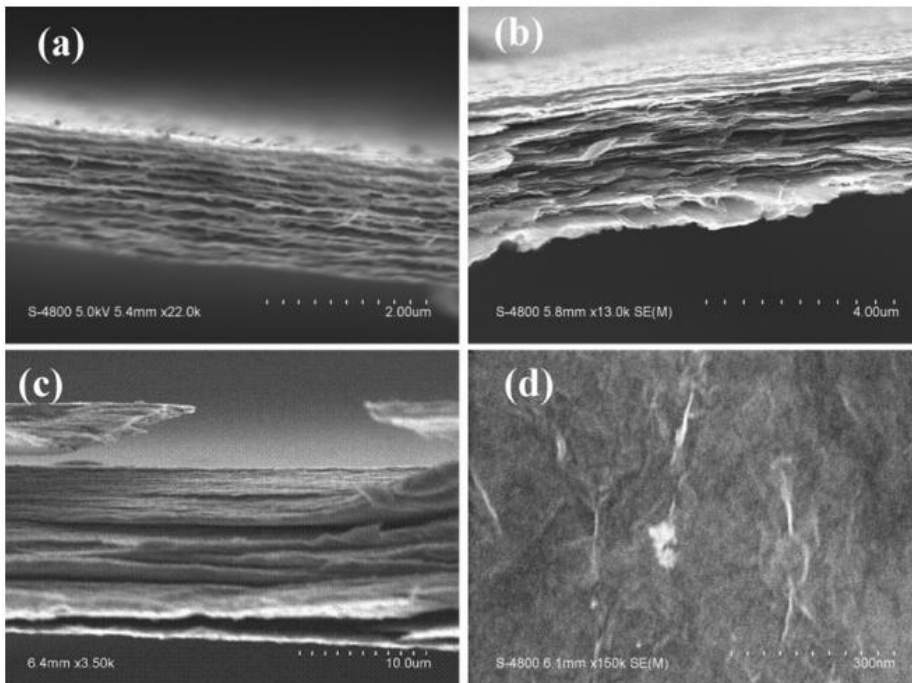


**Figure 13** SEM images of graphene papers: (a–c) cross sections of 1.5, 3 and 10 μm graphene paper, respectively; (d) top view of 10 μm graphene paper. (from Ref. 93. Y. Hu et al., *Electrochim. Acta*, 2013, 91, 227.)

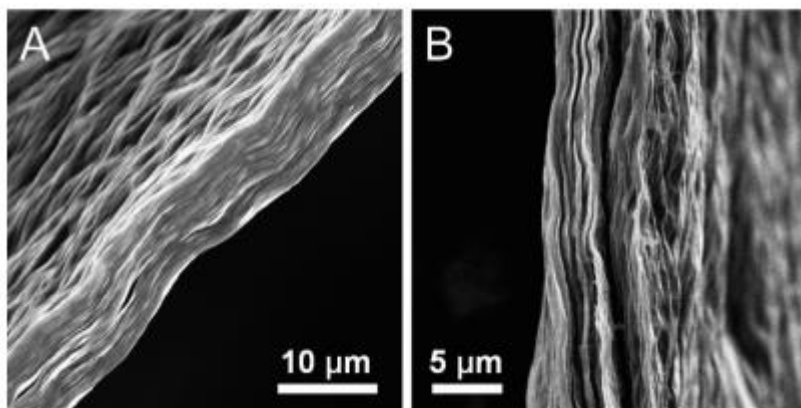


**Figure 14** SEM images of graphene paper showing the (A) undulating paper surface and (B) local heterogeneities along a fractured edge. (from Ref. 94. A. Abouimrane et al., *J. Phys. Chem. C*, 2010, 114, 12800.)

### **2.2.3. Graphene/metal oxide as an electrode**

Graphene holds considerable promise as a new anode material in LIBs due to its unique physical and chemical properties including: (1) superior electrical conductivity to graphitic carbon; (2) high surface area - the theoretical specific surface area of monolayer graphene is  $2630 \text{ m}^2 \text{ g}^{-1}$ ; (3) a high surface to volume ratio, which provides more active sites for ion adsorption and/or electrochemical reactions; (4) ultrathin thickness that obviously shortens the diffusion distance of ions; (5) structural flexibility that paves the way for constructing flexible electrodes; (6) thermal and chemical stability which guarantee its use in harsh environments; (7) abundant surface functional groups which make it hydrophilic in aqueous electrolytes, and provide binding sites with other atoms or functional groups; and (8) a broad electrochemical window that is critical for increasing energy density, which is proportional to the square of the window voltage.

Due to the limited capacity of graphite, many efforts have been focused on finding substitutes with larger capacity and slightly more positive intercalation voltage compared to  $\text{Li}/\text{Li}^+$ , so as to reduce the possible safety problems of lithium plating. Metal oxides, typically providing a capacity more than two times larger than that of graphite

with higher potential, have aroused wide interest [97]. The electrode reaction mechanism of metal oxides can be typically classified into three groups [98-100]: (1) conversion reaction, (2) Li-alloy reaction, and (3) Li insertion/extraction reaction. The conversion reaction mechanism is as follows:



where M is a metal such as Sn, Co, Ni, Fe, Cu, and Mn, and the final product consists of a homogeneous distribution of metal nanoparticles embedded in a Li<sub>2</sub>O matrix. However, their application in practical LIBs is significantly hindered by the poor cyclic performance arising from huge volume expansion and severe aggregation of metal oxides during charge/discharge. Another drawback is the large voltage hysteresis between charge and discharge together with poor energy efficiency. The Li-alloy reaction mechanism is as follows:



For example, a tin-based oxide first follows the conversion reaction mentioned above forming  $\text{Li}_2\text{O}$  and metallic tin, subsequently, the in-situ formed tin distributed in  $\text{Li}_2\text{O}$  can store and release lithium ions according to Li–Sn alloying/de-alloying reactions up to the theoretical limit of  $\text{Li}_{4.4}\text{Sn}$  corresponding to a theoretical reversible capacity of  $782 \text{ mAh g}^{-1}$  based on the mass of  $\text{SnO}_2$ . However, its poor cyclic performance caused by large volume changes (up to 300%) during charge/discharge leads to mechanical disintegration and the loss of electrical connection of the active material from current collectors. Li insertion/extraction reaction mechanism involves the insertion and extraction of  $\text{Li}^+$  into and from the lattice of the metal oxide which can be described as follows:



For instance,  $\text{TiO}_2$  is a common anode metal oxide follows a typical Li intercalation process with a volume change smaller than 4% in the reaction:  $\text{TiO}_2 + x\text{Li}^+ + x\text{e}^- \leftrightarrow \text{Li}_x\text{TiO}_2$  ( $0 \leq x \leq 1$ ). The lithium intercalation and extraction process with a small lattice change ensures its structural stability and cycling life. The lithium

intercalation potential is about 1.5 V, thus intrinsically maintaining the safety of the electrode through the avoidance of electrochemical Li deposition. However, its drawback is low specific capacity, poor lithium ionic and electronic conductivity and high polarization, resulting from the slow ionic and electronic diffusion of bulk TiO<sub>2</sub>. In supercapacitors, metal oxides provide higher pseudo-capacitance through bulk redox reactions compared with surface charge storage of carbonaceous materials. However, the large volume variation induced structure change breaks the stability of electrode materials, causing the rapid capacity loss during charge/discharge processes. Lithium can react with metallic/semimetallic elements and metal alloys, such as Si, Sn, Ge, Bi, Cu–Sn, and Ni–Sn showing high capacity, while their applications are facing the same challenge as metal oxides of large volume change during Li alloying/dealloying processes, which leads to the severe capacity fading. The comparison of above properties for graphene, metal oxides and graphene/metal oxide composites is summarized in **Table 2**.

Several structural models of graphene/metal oxide composites are proposed (**Figure 15**): (a) nano-sized oxides anchoring on graphene for LIBs (SnO<sub>2</sub> [101-103], Co<sub>3</sub>O<sub>4</sub> [104, 105], Fe<sub>2</sub>O<sub>3</sub> [106], Mn<sub>3</sub>O<sub>4</sub> [17],

MnO [107], Fe<sub>3</sub>O<sub>4</sub> [108]); (b) graphene-wrapped metal oxide particles (Fe<sub>3</sub>O<sub>4</sub> [109], TiO<sub>2</sub> [110]); (c) graphene-encapsulated metal oxides for LIBs (Co<sub>3</sub>O<sub>4</sub> [111], Fe<sub>3</sub>O<sub>4</sub> [112]); (d) a two-dimensional (2D) sandwich-like model: graphene as a template for the creation of a metal oxide/GNS sandwichlike structure (such as Co<sub>3</sub>O<sub>4</sub> [113], TiO<sub>2</sub> [114]); (e) graphene/metal oxide layered composites composed of aligned layers of metal oxide (TiO<sub>2</sub> [115], MnO<sub>2</sub> [116])-anchored graphene; (f) three-dimensional (3D) graphene (normally  $\leq 10$  wt% in composite) conductive networks among metal oxides (Li<sub>4</sub>Ti<sub>5</sub>O<sub>12</sub> [117], LiFePO<sub>4</sub> [118]).

**Table 2** The pros and cons of graphene, metal oxides, and graphene/metal oxide composites in LIBs and Ecs.

Pros of graphene	Cons of graphene	Pros of MO	Cons of MO	Pros of graphene/MO composites
Superior electrical conductivity	Serious agglomeration	Very large capacity/capacitance	Poor electrical conductivity	Synergistic effects
Abundant surface functional groups	Re-stacking	High packing density	Large volume change	Suppressing the volume change of MO
Thermal and Chemical stability	Large Irreversible capacity	High energy Density	Severe aggregation/agglomeration	Suppressing agglomeration of MO and re-stacking of graphene
Large surface area	Low initial coulombic efficiency	Rich resources	Large irreversible capacity	Uniform dispersion of MO
High surface-to-volume ratio	Fast capacity fading		Low initial coulombic efficiency	Highly conducting and flexible network
Ultrathin thickness	No clear lithium storage mechanism		Poor rate capability	High capacity/capacitance, good rate capability
Structural flexibility	No obvious voltage plateau		Poor cycling stability	Improved cycling stability
Broad electrochemical window	Large voltage hysteresis			Improved energy/power densities

MO: Metal oxides.

**Table 2** The pros and cons of graphene, metal oxides and graphene/metal oxide composites in LIBs. (from Ref. 35. Z. S. Wu et al., *Nano Energy*, 2012, 1, 107.)

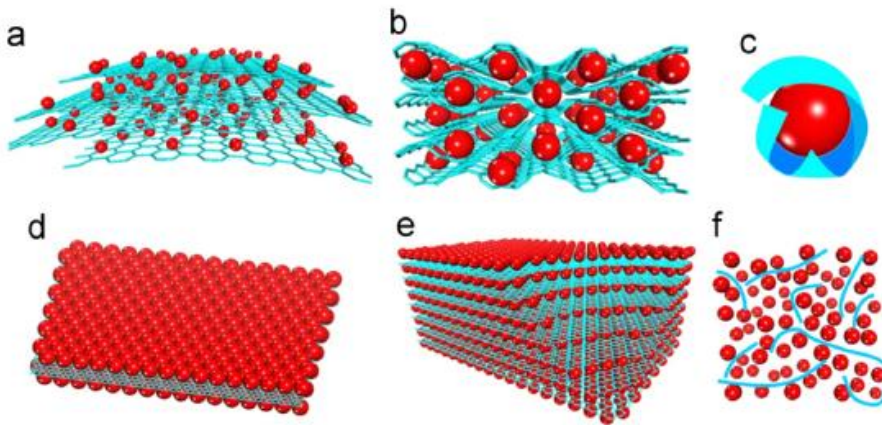


**Figure 15** Schematic of structural models of graphene/metal oxide composites: (a) Anchored model: nanosized oxide particles are anchored on the surface of graphene. (b) Wrapped model: metal oxide particles are wrapped by graphene. (c) Encapsulated model: oxide particles are encapsulated by graphene. (d) Sandwich-like model: graphene serves as a template for the creation of a metal oxide/graphene/metal oxide sandwich-like structure. (e) Layered model: a structure composed of alternating layers of metal oxide nanoparticles and graphene. (f) Mixed model: graphene and metal oxide particles are mechanically mixed and graphene forms a conductive network among the metal oxide particles. Red: metal oxide particles; Blue: graphene sheets. (from Ref. 35. Z. S. Wu et al., *Nano Energy*, 2012, 1, 107.)

## **2.3. Challenges to problems**

### **2.3.1. Restacking of graphene paper**

It is essential to make clear the origin of the phenomenon in order to explain the restacking issue of graphene sheets. In Hummer's method, it is notorious that one or a few layers of GO are highly dispersed in the aqueous solution [119, 120]. Interestingly, even after the GO solution is dried, water molecules stuck in the GO powder are interacted with oxygen-containing functional groups of GO via hydrogen bonding and these water molecules are generally referred to as intercalated water molecules like lithium ions [121]. These water molecules decisively play a crucial role in the restacking of the final rGO (**Figure 16**) because the hydrogen bonding facilitates interactions between GO sheets, resulting in aligning the GO sheets in the same orientations [122].

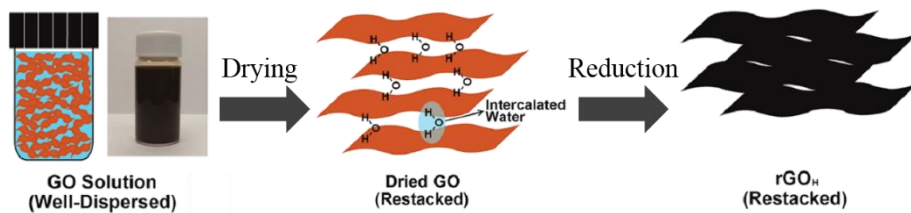


**Figure 16** Schematic illustrations showing restacking of graphene oxide and graphene. (from Ref. 122. J. H. Lee et al., *ACS Nano*, 2013, 7, 9366.)

### **2.3.2. Improvement of lithium ion and electron transport for rate capability**

Extremely large aspect ratio of graphene sheets places constraint on the practical capacity of graphene-based electrodes at high charge/discharge rates. During drying of randomly stacked graphene sheets, the surface tension of the retreating liquid meniscus collapses the spacing between sheets and leads to intimate van der Waals contact between them, hence reducing open porosity [95]. Thermally annealed graphene stacks show severe intersheet aggregation that limits permeation of electrolyte between the layers. Thus, in spite of a high in-plane Li diffusion coefficient of  $\sim 10^{-8} \text{ cm}^2 \text{ s}^{-1}$ , cross-plane diffusivity is low, and Li migration into and out of a graphene stack is restricted to stack edges. In-plane pores (**Figure 17 and 18**) provide a high density of new, cross-plane ion diffusion channels that facilitate charge transport and storage at high rates [54]. Combining this with a 3D graphitic architecture that maintains superior electrical conductivity and structural integrity (**Figure 19**), a novel form of graphene electrode is generated, which is capable of ultrahigh power delivery [123].

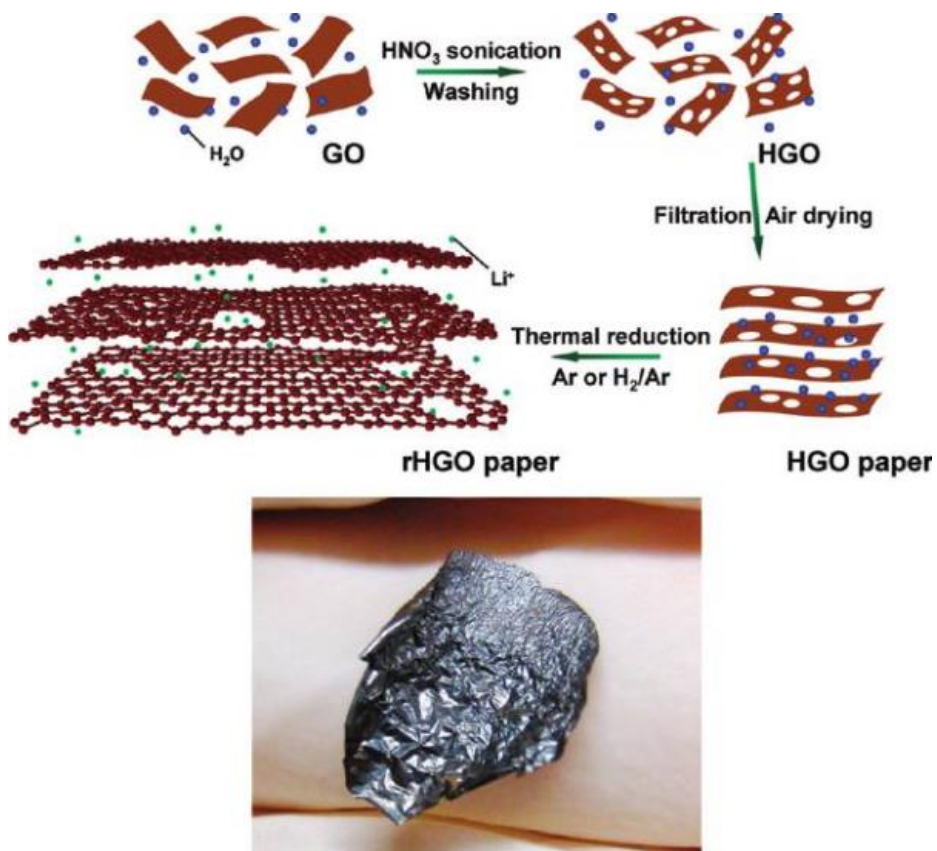


**Figure 17** Schematic drawing of the introduction of in-plane pores into chemically exfoliated graphene oxide and the subsequent filtration into a holey graphene oxide paper. (from Ref. 95. X. Zhao et al., *ACS Nano*, 2011, 5, 8739.)

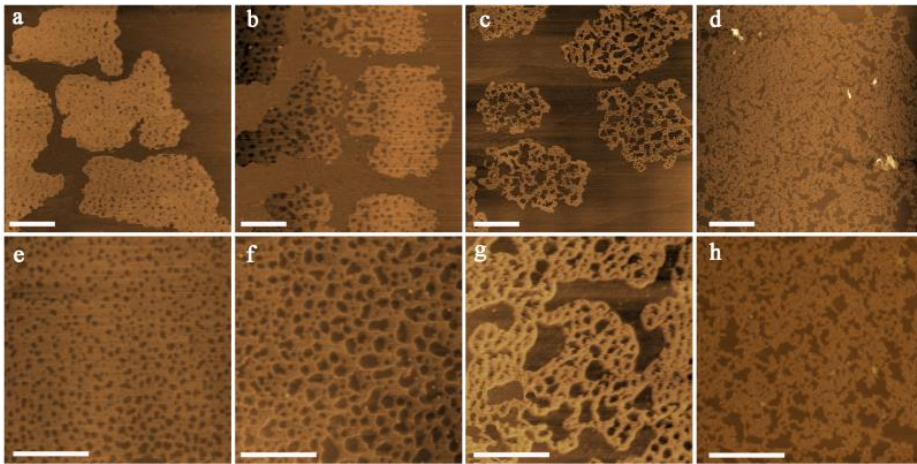


**Figure 18** The evolution of nanopores; (a–d) scale bar = 2  $\mu\text{m}$  and (e–h) scale bar = 1  $\mu\text{m}$ . (from Ref. 54. X. Wang et al., *Sci. Rep.*, 2013, 3. 1996.)

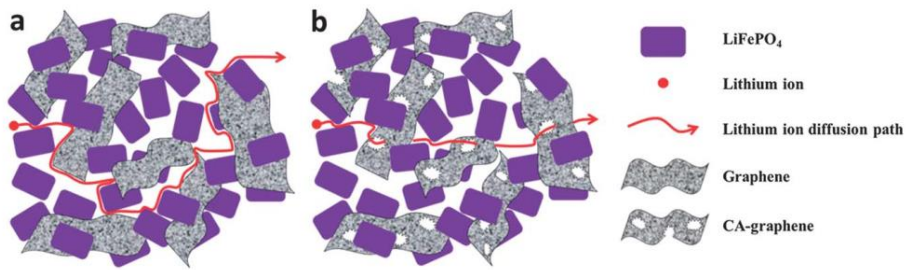


**Figure 19** Conceptual illustrations of lithium ion diffusion pathways in (a) G/LFP and (b) CA-G/LFP. (from Ref. 123. J. Ha et al., *Nanoscale*, 2013, 5, 8647.)

## **Chapter 3. Experiments**

### **3. Experiments**

#### **3.1. Materials**

Graphite powder (< 20 micron, synthetic), phosphorus pentoxide ( $P_2O_5$ , 97%), potassium permanganate ( $KMnO_4$ , 99.3%), Tin (IV) chloride pentahydrate ( $SnCl_4 \cdot 5H_2O$ , 98%), hydrazine monohydrate ( $N_2H_4$ , 80 wt%) and sulfuric acid ( $H_2SO_4$ , 95–98%) from Aldrich and hydrochloric acid ( $HCl$ , 35.0–37.0%), hydrogen peroxide ( $H_2O_2$ , 30.0–35.5%), polyethylene glycol #400 ( $H(OCH_2CH_2)_nOH$ ), potassium persulfate ( $K_2S_2O_8$ , 98.0%), from SAMCHUN were purchased, respectively. All reagents were used without further purification. An Anodisc membrane filter (47 mm in diameter, Whatman) with pore size of 0.2  $\mu m$  was used for the preparation of the pristine and composite paper by vacuum filtration. Water Purification System produced 18.2 M  $\Omega$  deionized water was used throughout the experiments.

#### **3.2. Synthesis of graphene oxides and acid-treated graphene oxides**

GO was synthesized from commercial graphite by the modified Hummers' method. The synthesis of GO consisted of two steps which are pre-oxidation and oxidation. Briefly, in the pre-oxidation, graphite was mixed with  $K_2S_2O_8$ ,  $P_2O_5$ , and  $H_2SO_4$ . This mixture was stirred at 95 °C for 5 h. After cooling down, it was washed with DI water

several times and then dried at 60 °C overnight. In the oxidation step,  $\text{KMnO}_4$  was slowly added to pre-oxidized graphite with  $\text{H}_2\text{SO}_4$  in an ice bath during agitation. After it was stirred at 80 °C for 4 h,  $\text{H}_2\text{O}_2$  was added to the mixture. The color of the mixture changed from dark brown to yellow. Finally, the resulting product was washed and rinsed with HCl aqueous solution (1:10 volume ratio) and DI water, followed by drying in an electric oven at 60 °C for 24 h. Acid-treated graphene oxide (AGO) was synthesized by using the process developed by Shi's group. Typically, 250 mg of GO was immersed in 250 ml of nitric acid solution (4 M) and refluxed at 100 °C for 1 hour. The resulting solution was washed several times with DI water to neutralize, and then it was freeze-dried.

### **3.3. Synthesis of MnOOH nanorods**

$\text{KMnO}_4$ , polyethylene glycol 400 (PEG-400) and DI water were used to synthesize MnOOH nanorods (MnOOH NRs). Typically, 0.3 g of  $\text{KMnO}_4$  and 7.5 ml of PEG-400 in 60 ml of DI water were stirred at room temperature for 30 min, after which the solution turned dark brown. It was then transferred into a 100 mL Teflon-lined stainless steel autoclave and heated at 160 °C for 3 h in an electric oven. The brownish product was washed with DI water and ethanol several times.

### **3.4. Fabrication of pMn<sub>3</sub>O<sub>4</sub> NR/rGO paper**

A uniform composite paper was fabricated using vacuum-assisted filtration. For the preparation of the MnOOH nanorod/graphene oxide (MnOOH NR/GO) suspension, GO was dispersed in DI water (1 mg mL<sup>-1</sup>) using ultrasonication for 1 h and centrifugation at 3000 rpm for 30 min. After centrifugation, a supernatant was mixed with MnOOH NRs, followed by ultrasonication for 1 h. The homogeneous MnOOH NR/GO suspension was filtered with an Anodisc membrane filter (47 mm in diameter, 0.2 μm pore size, Whatman). The obtained MnOOH NR/GO paper was dried at room temperature overnight and peeled from the filter. For the phase transformation of MnOOH and the reduction of GO, the as-prepared composite paper was heated at 400 °C for 2 h under N<sub>2</sub> gas. Finally, a pMn<sub>3</sub>O<sub>4</sub> NR/rGO paper was obtained.

### **3.5. Fabrication of Mn<sub>3</sub>O<sub>4</sub> NR, rGO/Mn<sub>3</sub>O<sub>4</sub> NR and ArGO/Mn<sub>3</sub>O<sub>4</sub> NR**

Mn<sub>3</sub>O<sub>4</sub> NR, rGO/Mn<sub>3</sub>O<sub>4</sub> NR and ArGO/Mn<sub>3</sub>O<sub>4</sub> NR were fabricated using a simple mixing and heat treatment. GO (or AGO) and MnOOH NRs (3:1 weight ratio) were homogeneously dispersed in DI water using sonication for 30 min followed by drying at 60 °C in an electric

oven. The bare and mixed powders were heated in a tube furnace at 400 °C for 5 h under N<sub>2</sub> atmosphere.

### **3.6. Synthesis of SnO<sub>2</sub>, rGO /SnO<sub>2</sub> and ArGO/SnO<sub>2</sub>**

rGO/SnO<sub>2</sub> (GS) and ArGO/SnO<sub>2</sub> (AGS) nanocomposites were prepared by the following procedure presented in **Figure 38**. 0.2 g of GO (or AGO) and 0.7 g (2 mmol) of Tin (IV) chloride in 60 mL of DI water were sonicated for 30 min. Then, 485 μL of hydrazine monohydrate was added to mineralize the tin ions while the solution was vigorously agitated for 15 min. The mixture was transferred into 100 ml of a Teflon-lined stainless steel autoclave and reacted hydrothermally at 160 °C for 12 h. The autoclave was slowly cooled down to room temperature, and a black-colored product was washed and isolated by filtration and freeze-dried overnight.

For comparison, bare SnO<sub>2</sub> nanoparticles were prepared by a hydrothermal method. First, 1.4 g (4 mmol) of Tin (IV) chloride pentahydrate in 60 mL of DI water was agitated until a solution was transparent. Next, 0.97 mL of hydrazine monohydrate was added to the solution while it was agitated for 15 min. The opaque white solution was transferred into a Teflon-lined stainless steel autoclave

and reacted at 160 °C for 12 h. Finally, the resulting white product was centrifuged and freeze-dried overnight.

### **3.7. Material characterization**

The morphologies of all samples were characterized using high resolution transmission electron microscopy (HR-TEM, JEOL JEM 2100F) at an accelerating voltage of 200 kV. The cross-sectional morphology and surfaces of samples were examined by field-emission scanning electron microscopy (FE-SEM, Hitachi S-4800) with an accelerating voltage of 0.5–30 kV. Crystallographic studies were performed using an X-ray diffractometer (XRD, BRUKER D8 Advance) with Cu K $\alpha$  radiation ( $\lambda = 1.54 \text{ \AA}$ ) from 10° to 80° at a scan rate of 2° min<sup>-1</sup>. Thermogravimetric analysis (TGA, Mettler Toledo TGA/DSC 1) was performed from 25 to 750 °C at a heating rate of 10 °C min<sup>-1</sup> in air. Fourier transform infrared spectra (FT-IR, ThermoFisher Nicolet 5700) were recorded from 400 to 4000 cm<sup>-1</sup>. Brunauer–Emmett–Teller (BET) specific surface areas (SSA) and pore-size distribution were calculated by N<sub>2</sub> absorption/desorption isotherms on a BELSORP apparatus and Barrett–Joyner–Halenda (BJH) method, respectively.

### **3.8. Electrochemical measurements**

The electrochemical performance of the samples as anodes was obtained by using CR2016-type coin cells with a Li foil as the counter and reference electrodes. The electrolyte was 1M LiPF<sub>6</sub> solution in a mixture of ethylene carbonate and dimethyl carbonate (1:1 in volume). The rGO and pMn<sub>3</sub>O<sub>4</sub> NR/rGO composite papers, which were used directly as the working electrodes, were cut into the desired size and applied without any additional conductive material or binder. The papers were dried overnight in a vacuum oven at 120 °C. The cells were assembled in an Ar-filled glove box and then galvanostatically tested at 100 mA g<sup>-1</sup> in the voltage range of 0.05–3.0 V versus Li/Li<sup>+</sup>. Cyclic voltammetry (CV) testing was carried out at a scan rate of 0.1 mV s<sup>-1</sup> in the potential range of 0.05–3.0 V.

Mn<sub>3</sub>O<sub>4</sub> NR, rGO/Mn<sub>3</sub>O<sub>4</sub> NR and ArGO/Mn<sub>3</sub>O<sub>4</sub> NR electrodes were fabricated by mixing 70 wt% of active material (samples), 10 wt% of binder (PVDF) and 20 wt% of conductive carbon (Super P). These materials were mixed with the n-methyl-2-pyrrolidinone (NMP) and coated onto the Cu foil by a doctor blade. After drying at 60 °C in a vacuum oven for 2 h, the coated foil was compressed and cut into circular electrodes. Electrodes were dried overnight at 120 °C in a vacuum oven and transferred to an Ar-filled glove box. All the cells

were galvanostatically tested at  $200 \text{ mA g}^{-1}$  between 0.01 and 3.0 V versus  $\text{Li/Li}^+$  (WBCS3000 cycler system, Wonatech, Korea). Cyclic voltammetry (CV) tests were also conducted at a scan rate of  $0.1 \text{ mV s}^{-1}$  between 0.01 and 3.0 V.

The working electrodes, which are  $\text{SnO}_2$ , GS and AGS, were fabricated by homogeneously mixing 70 wt% of active material, 15 wt% of PVDF and 15 wt% of Super P with NMP and coating the slurry onto the Cu foil by a doctor blade. The coated foil was pressed after it is dried at  $60 \text{ }^\circ\text{C}$  in a vacuum oven for 2 h. Circular electrodes were dried overnight at  $120 \text{ }^\circ\text{C}$  in a vacuum oven and transferred to argon-filled glove box. The cells were assembled and then galvanostatically tested at 200 and  $500 \text{ mA g}^{-1}$  in the voltage range of 0.01–2.0 V versus  $\text{Li/Li}^+$  (WBCS3000 cycler system, Wonatech, Korea). Cyclic voltammetry (CV) testing was carried out at a scan rate of  $0.1 \text{ mV s}^{-1}$  in the potential range of 0.01–2.0 V.

## **Chapter 4. Results and Discussion**

#### **4.1. Porous Mn<sub>3</sub>O<sub>4</sub> Nanorod/Reduced Graphene Oxide Hybrid Paper as a Flexible and Binder-free Anode Material for Lithium Ion Battery**

The fabrication process for pMn<sub>3</sub>O<sub>4</sub> NR/rGO paper is depicted in **Figure 20**. The as-prepared MnOOH NRs were well dispersed on the surface of GO under sonication. After vacuum filtration, a flexible, free-standing MnOOH NR/GO paper was obtained. Finally, the MnOOH NR/GO paper was reduced to pMn<sub>3</sub>O<sub>4</sub> NR/rGO paper by a thermal treatment. This transformation could be observed via SEM, TEM, and XRD.

**Figure 21** and **Figure 22** display the cross-section and top-view SEM images of the samples, respectively. The GO paper has a lamellar, rough and wavy structure, as previously reported (**Figure 21a**). It also shows a densely stacked structure with a thickness of ~10 μm due to the hydrogen bond network between water and oxygen-containing functional groups on the surface of GO, which are carboxyl, carbonyl, epoxy, and hydroxyl groups. An undulating surface morphology can be observed in the top-view image of the GO paper (**Figure 22a**). As shown in **Figure 21b**, MnOOH NRs are well intercalated between GO layers, resulting in the formation of a 3D

structure. This 3D structure can provide the pathway for  $\text{Li}^+$  diffusion and a large contact area between the active materials and electrolytes. Furthermore, **Figure 22b** clearly reveals that  $\text{MnOOH}$  NRs (**Figure 27a**) are homogeneously dispersed in the composites paper and are continuously interconnected within GO layers.

The cross-sectional SEM images of  $\text{pMn}_3\text{O}_4$  NR/rGO paper are presented in **Figure 21c** and **d**. The morphology of  $\text{pMn}_3\text{O}_4$  NR/rGO paper is quite similar to that of  $\text{MnOOH}$  NR/GO paper, indicating that the  $\text{MnOOH}$  NR/GO paper is completely transformed to  $\text{pMn}_3\text{O}_4$  NR/rGO paper without the deformation of nanorods. Furthermore, the  $\text{pMn}_3\text{O}_4$  NR/rGO paper has a loosely stacked layer structure with open voids. Interestingly, after heat treatment, the  $\text{Mn}_3\text{O}_4$  NRs (**Figure 27b**) have inner pores with diameters of 10–20 nm. As previously reported, the formation of the porous structures is due to the release of gases such as  $\text{H}_2\text{O}$  and  $\text{O}_2$  during  $\text{MnOOH}$  decomposition. For that reason, the  $\text{Mn}_3\text{O}_4$  NRs possess the porosity in the structure (red circles). This 1D porous structure provides a short  $\text{Li}^+$  diffusion path and 1D electron transport along the nanorods. Consequently, it is anticipated that the porous structure of the  $\text{pMn}_3\text{O}_4$  NR/rGO paper is favorable to an effective lithium ion diffusion and wettability of electrolytes over

the entire composite paper. The flexibility of as-prepared  $\text{pMn}_3\text{O}_4$  NR/rGO paper is given in the inset of **Figure 22d**. This graphene-based composite paper could play an important role in developing flexible, wearable and thin film devices, especially LIBs.

The crystalline structures and shapes of MnOOH NR/GO and  $\text{pMn}_3\text{O}_4$  NR/rGO paper were further characterized by TEM and high-resolution TEM (HR-TEM), as shown in **Figure 23**. In TEM images of the MnOOH NR/GO paper, highly crystalline MnOOH NRs with diameters of 60–120 nm are deposited well to the surface of GO sheets (**Figure 23a**). After heat treatment, porous  $\text{Mn}_3\text{O}_4$  NRs were obtained without size variation, which is in good agreement with the SEM images (**Figure 23b**). At higher magnification, pores in  $\text{Mn}_3\text{O}_4$  NRs were clearly observed (**Figure 23e**, red circles). In addition, small-sized  $\text{Mn}_3\text{O}_4$  nanoparticles were grown on the surface of rGO sheets due to the redox reaction between GO and MnOOH NRs during the thermal reaction.

In an HR-TEM image of  $\text{pMn}_3\text{O}_4$  NR/rGO paper, a porous  $\text{Mn}_3\text{O}_4$  NR clearly shows 0.3 and 0.27 nm d-spacing, which correspond to the (112) and (103) planes, respectively. In addition, fast Fourier transform (FFT) patterns (inset of **Figure 23c**) indicate highly crystalline multi-domains

in the porous  $\text{Mn}_3\text{O}_4$  NR. The chemical compositions of porous  $\text{Mn}_3\text{O}_4$  NR were also characterized by elemental mapping analysis (**Figure 23f**). The  $\text{pMn}_3\text{O}_4$  NR/rGO paper is mainly composed of carbon, manganese, and oxygen.

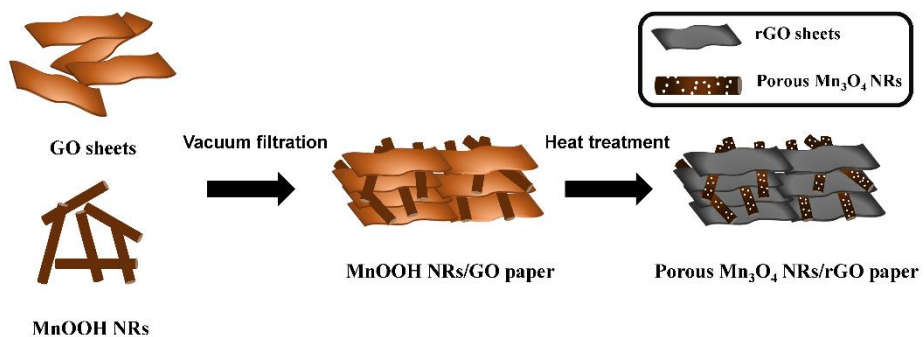


**Figure 20** Schematic illustration of the synthesis of pMn<sub>3</sub>O<sub>4</sub> NR/rGO paper.

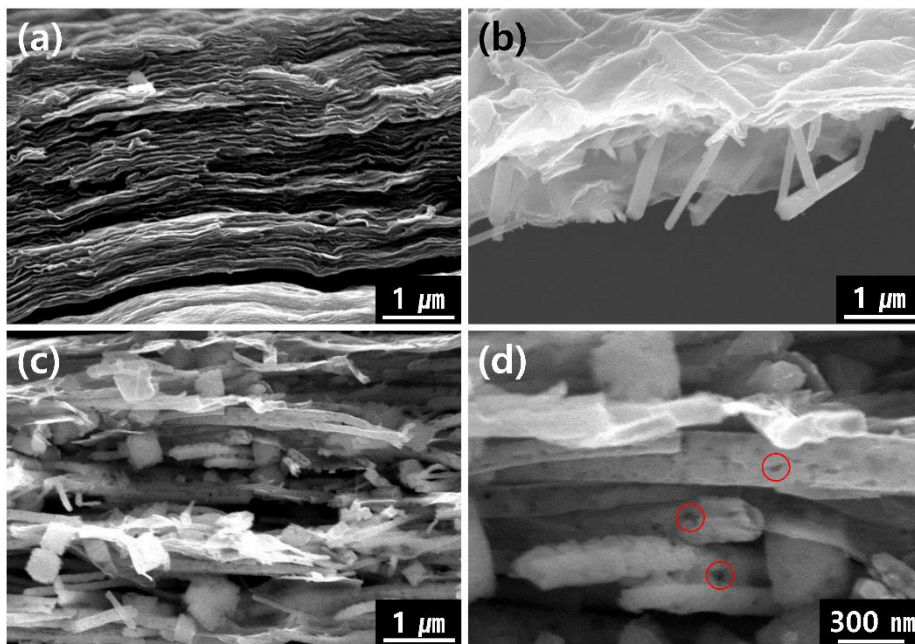


**Figure 21** Cross-sectional SEM images of GO paper (a), MnOOH NR/GO paper (b) and pMn<sub>3</sub>O<sub>4</sub> NR/rGO paper (c and d).

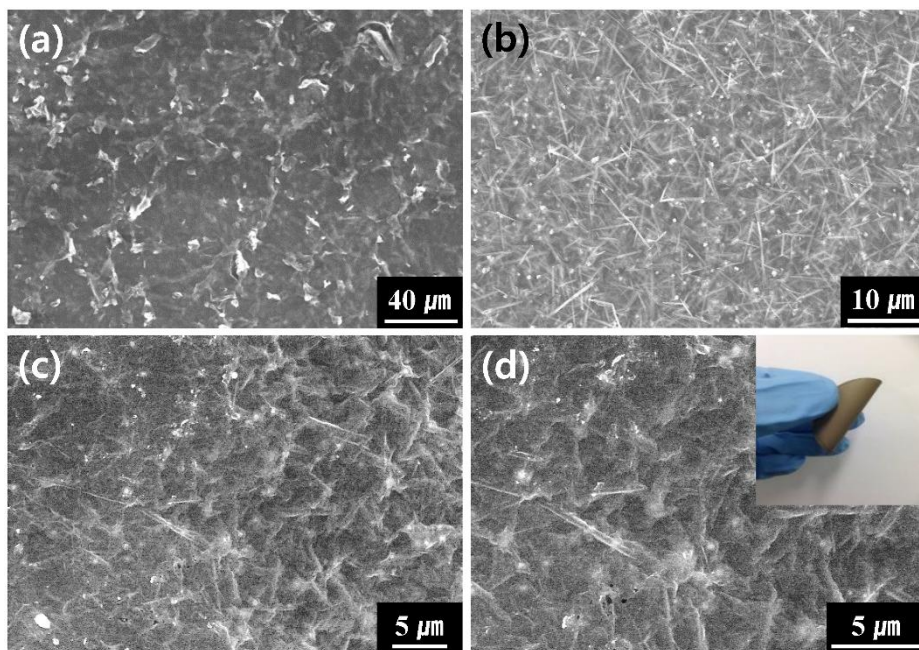


**Figure 22** Top-view SEM images of GO paper (a), MnOOH NR/GO paper (b) and pMn<sub>3</sub>O<sub>4</sub> NR/rGO paper (c and d).

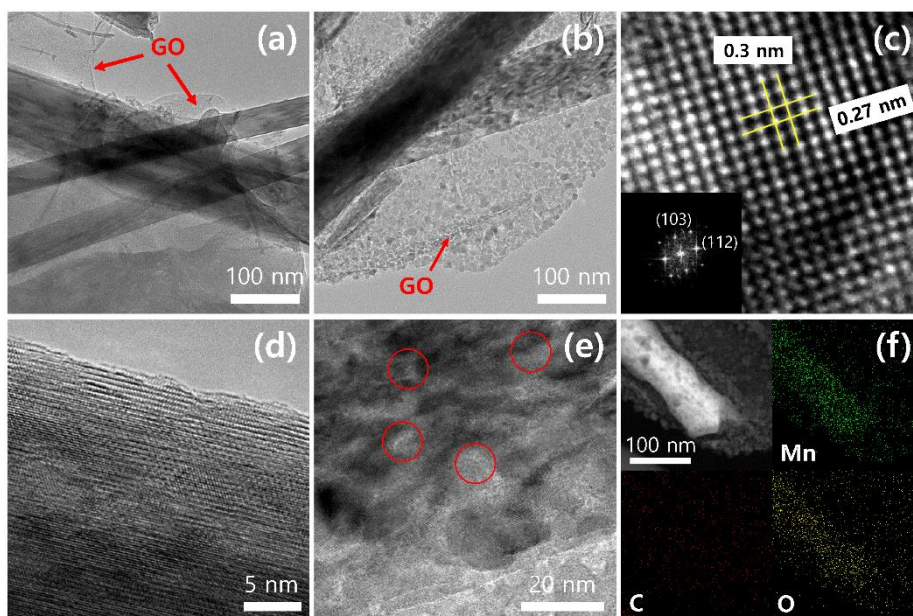


**Figure 23** TEM and HRTEM Images of MnOOH NR/GO paper (a and d) and pMn<sub>3</sub>O<sub>4</sub> NR/rGO paper (b, c, and e). (f) Dark-field TEM image and the corresponding Mn, C, and O element mapping.

The X-ray diffraction patterns of rGO and GO paper are presented in **Figure 24a**. As shown in **Figure 24a**, the GO paper has an intense and sharp diffraction peak at  $2\theta = 11^\circ$ , corresponding to the characteristic (001) diffraction of GO. After thermal treatment, a new broad diffraction peak attributed to a typical (002) pattern of amorphous carbon appeared at  $2\theta = 22^\circ$ . The broadened peak of rGO indicates that the GO paper was successfully reduced to rGO paper. Due to the successful reduction of GO paper, the rGO paper can be used as a current collector without a binder and a flexible substrate for LIBs.

The crystalline structures of MnOOH NR/GO and pMn<sub>3</sub>O<sub>4</sub> NR/rGO paper were also characterized by XRD. In **Figure 24b**, the diffraction peaks of MnOOH NR/GO paper obtained by vacuum filtration correspond to a mixed phase of  $\gamma$ -MnOOH and Mn<sub>3</sub>O<sub>4</sub>. It reveals that manganese oxide materials in the MnOOH NR/GO paper consist predominantly of  $\gamma$ -MnOOH and some Mn<sub>3</sub>O<sub>4</sub> NRs. The XRD peaks of pMn<sub>3</sub>O<sub>4</sub> NR/rGO paper also correspond to Mn<sub>3</sub>O<sub>4</sub> (Hausmannite, JCPDS No. 24-0734) phase, indicating that the MnOOH NR/GO paper is completely transformed to pMn<sub>3</sub>O<sub>4</sub> NR/rGO paper by heat treatment. The diffraction peaks at  $18.0^\circ$ ,  $28.7^\circ$ ,  $31.0^\circ$ ,  $32.3^\circ$ ,  $36.1^\circ$

and  $36.4^\circ$  can be matched to (101), (112), (200), (103), (211) and (202) planes of the tetragonal  $\text{Mn}_3\text{O}_4$ . The results are similar with that of previous studies. The peaks of rGO are not observed due to its low content and intensity compared to those of  $\text{Mn}_3\text{O}_4$  NRs.

To confirm the reduction of GO and the existence of manganese oxide after thermal treatment, FT-IR spectra of MnOOH NR/GO and pMn<sub>3</sub>O<sub>4</sub> NR/rGO composite papers were recorded (**Figure 25a**). In the FT-IR spectrum of pMn<sub>3</sub>O<sub>4</sub> NR/rGO paper, it is clearly observed that the oxygen-containing groups in GO were nearly removed after thermal treatment. Specifically, the IR spectrum of MnOOH/GO paper shows O–H at  $1400\text{ cm}^{-1}$  (carboxyl group), C–O at  $1080\text{ cm}^{-1}$  (epoxy group), C=O at  $1730\text{ cm}^{-1}$  (carboxyl and carbonyl groups) and C=C at  $1623\text{ cm}^{-1}$ , which are assigned to residual graphitic domains. On the contrary, the pMn<sub>3</sub>O<sub>4</sub> NR/rGO paper exhibited the C=C peak and a weak C–OH peak. In addition, both samples show very sharp peaks in the range of  $400\sim 700\text{ cm}^{-1}$  (black circle). The two absorption peaks at  $476$  and  $602\text{ cm}^{-1}$  can be assigned to the vibration of the Mn–O stretching modes in tetrahedral and octahedral sites of  $\text{Mn}_3\text{O}_4$  NR. The absorption peak at  $417\text{ cm}^{-1}$  is ascribed to the bond stretching modes and displacement of the  $\text{Mn}^{2+}$  ions, respectively, in the octahedral and

tetrahedral sites, which are negligible. The sharp and narrow peaks at 442, 486, and 590  $\text{cm}^{-1}$  are attributed to the vibrations of the Mn–O bonds in MnOOH NRs.

The  $\text{pMn}_3\text{O}_4$  NR content in the as-prepared paper was determined by TGA via oxidative decomposition (**Figure 25b**). The weight fraction of  $\text{pMn}_3\text{O}_4$  NRs in the composite paper is about 78%, indicating the successful fabrication of a composite paper with a high loading of metal oxide NRs. Below 200 °C, the TGA curve of the  $\text{pMn}_3\text{O}_4$  NR/rGO paper is mainly attributed to the loss of absorbed water. In the temperature range of 250–600 °C, the rGO starts to decompose into  $\text{CO}_2$ . There is no weight loss above 600 °C, demonstrating a residual weight ratio consistent with the content of  $\text{pMn}_3\text{O}_4$  NRs in the composites paper.

CV curves of  $\text{pMn}_3\text{O}_4$  NR/rGO paper at a scan rate of 0.1  $\text{mV s}^{-1}$  are shown in **Figure 26a**. During the first discharge cycle, a small reduction peak is observed at ~1.17 V, corresponding to formation of the solid electrolyte interphase (SEI) and decomposition of the electrolyte. The sharp cathodic peak at 0.13 V is assigned to the reduction reaction of  $\text{Li}^+$  with  $\text{pMn}_3\text{O}_4$  NRs and rGO. In the first charging process, the strong peak appearing at 1.3 V is attributed to

the oxidation of metallic manganese (Mn) to manganese ions. The electrochemical reaction mechanism (1) can be described as follows.



The subsequent CV curves (second and fifth) demonstrate that the charge/discharge reaction is reversible.

**Figure 26b** shows the charge/discharge profiles of the pMn<sub>3</sub>O<sub>4</sub> NR/rGO paper at a current density of 100 mA g<sup>-1</sup> over a voltage range of 0.05–3.0 V vs. Li/Li<sup>+</sup>. The slope in the range of 1.17–0.27 V is mainly due to the reduction from Mn<sup>3+</sup> to Mn<sup>2+</sup>, whereas the voltage plateau in the range of 0.27–0.13 V indicates the further reduction from Mn<sup>2+</sup> to Mn<sup>0</sup>. The sloping voltage at around 1.3 V during the charge is attributed to the oxidation from Mn<sup>0</sup> to Mn<sup>2+</sup> as a result of the reverse reaction between Li<sup>+</sup> and Mn<sub>3</sub>O<sub>4</sub> NRs. The first discharge and charge capacities are about 943 and 627 mA h g<sup>-1</sup>, respectively, with a Coulombic efficiency of 66.5%. The irreversible capacity loss may be related to various irreversible processes, such as the formation of a SEI layer and electrolyte decomposition. In the first discharge process, the main reduction reaction occurs at 0.27 V, which is in

accordance with the CV curve. After the first cycle, the main plateaus shift to a higher voltage ( $\sim 0.4$  V), which can be explained as lithium insertion becoming easier after the first cycle.

To obtain the cycle stability of the electrodes,  $\text{pMn}_3\text{O}_4$  NR/rGO and bare rGO paper were evaluated at  $100 \text{ mA g}^{-1}$  for 100 cycles (**Figure 26c**). Compared rGO paper, the  $\text{pMn}_3\text{O}_4$  NR/rGO paper delivers a high specific capacity  $573 \text{ mA h g}^{-1}$  after 100 cycles, indicating that the  $\text{pMn}_3\text{O}_4$  NRs contribute significantly to the specific capacity retention. The rGO in paper plays an important role in improving the cycling stability due to its superior electric conductivity and physicochemical stability. Therefore, the Coulombic efficiency of the composite paper at a current density of  $100 \text{ mA g}^{-1}$  is nearly 100% from the third cycle to subsequent cycles.

Furthermore, the  $\text{pMn}_3\text{O}_4$  NR/rGO and bare rGO paper were tested at various current densities to investigate the relationship between different rates with specific capacities from  $50$  to  $2000 \text{ mA g}^{-1}$ . As shown in **Figure 26d**, the  $\text{pMn}_3\text{O}_4$  NR/rGO paper delivers a high capacity of  $692$ ,  $618$ ,  $411$ ,  $313$ , and  $196 \text{ mA h g}^{-1}$  at  $50$ ,  $100$ ,  $500$ ,  $1000$ , and  $2000 \text{ mA g}^{-1}$ , respectively. Remarkably, as soon as the current density returned to  $50 \text{ mA g}^{-1}$ , the discharge capacity of

pMn<sub>3</sub>O<sub>4</sub>/rGO paper recovered to 752 mA h g<sup>-1</sup>. These results show that the lithium storage performance of pMn<sub>3</sub>O<sub>4</sub> NR/rGO paper is not affected by high current density. These performances could be attributed to the following factors. First, a binder-free electrode provides improved charge transfer kinetics because electrically insulating binders are not used. Second, the strong interfacial interactions between pMn<sub>3</sub>O<sub>4</sub> NR and rGO promote the interfacial lithium ion and electron transport considerably. On the other hand, rGO has excellent elasticity to effectively accommodate the volume expansion during cycling. Third, the porous structure of Mn<sub>3</sub>O<sub>4</sub> NRs and the pores within the pMn<sub>3</sub>O<sub>4</sub> NR/rGO paper can not only provide more active sites for the intercalation of Li<sup>+</sup> ions but also improve the contact of the paper to the electrolyte and shorten the diffusion pathways. These unique factors affect the high capacity, good rate capability and cycle stability of pMn<sub>3</sub>O<sub>4</sub> NR/rGO paper.

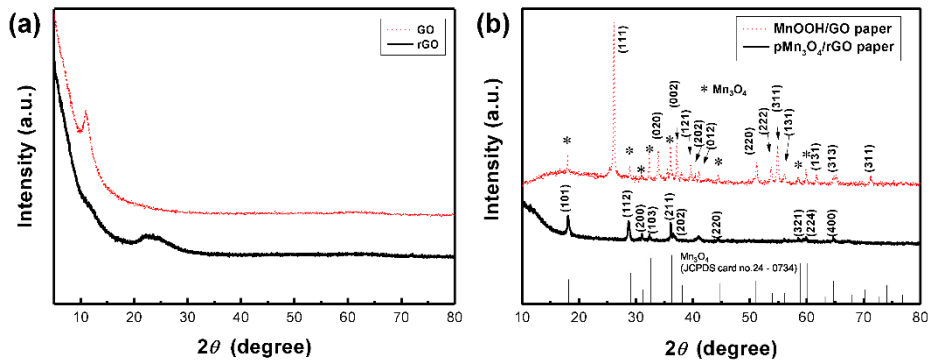


**Figure 24** (a) XRD patterns of GO and rGO and (b) MnOOH NR/GO paper and pMn<sub>3</sub>O<sub>4</sub> NR/rGO paper.

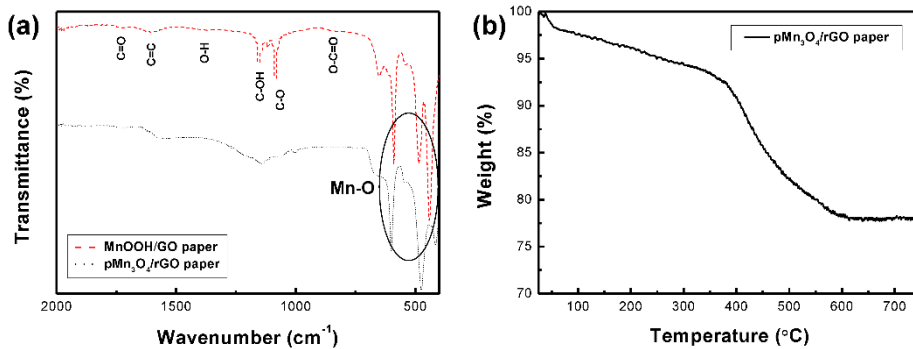


**Figure 25** (a) FT-IR transmittance spectra of pMn<sub>3</sub>O<sub>4</sub> NR/rGO and MnOOH NR/GO paper and (b) TGA curve of pMn<sub>3</sub>O<sub>4</sub> NR/rGO paper.

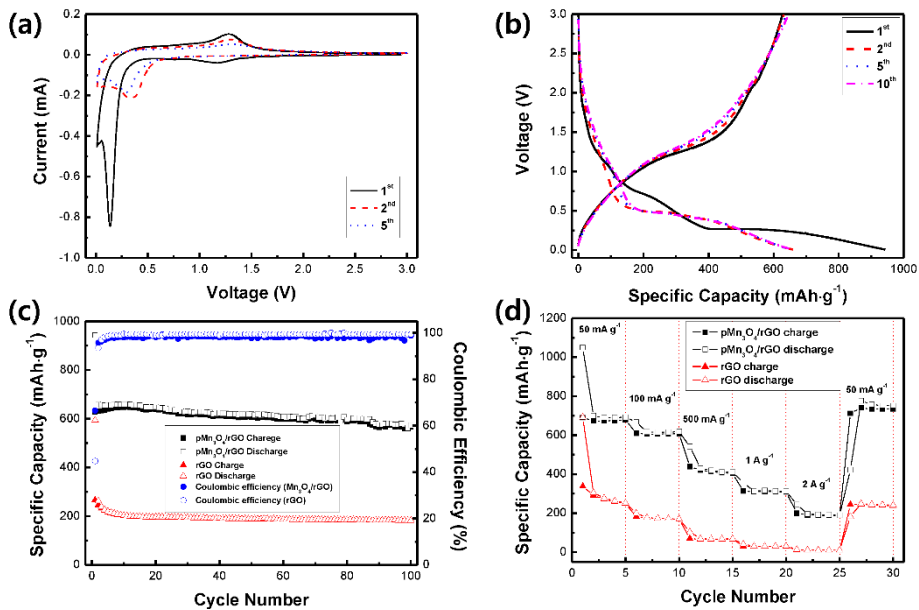


**Figure 26** (a) Cyclic voltammograms of pMn<sub>3</sub>O<sub>4</sub> NR/rGO paper at a scanning rate of 0.1 mV s<sup>-1</sup>, (b) charge–discharge profiles of pMn<sub>3</sub>O<sub>4</sub> NR/rGO paper, (c) comparative cycle performance of papers at a current density of 100 mA g<sup>-1</sup> and (d) rate capability of pMn<sub>3</sub>O<sub>4</sub> NR/rGO and bare rGO paper at various current densities.

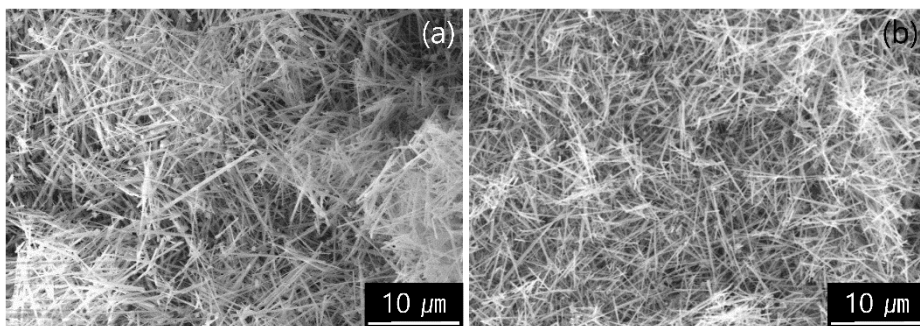


**Figure 27** (a) MnOOH nanorods and (b) Mn<sub>3</sub>O<sub>4</sub> nanorods after the thermal treatment.

## 4.2. An Acid-treated Reduced Graphene Oxide/Mn<sub>3</sub>O<sub>4</sub> Nanorod Nanocomposite as an Enhanced Anode Material for Lithium Ion Batteries

**Figure 29** shows the XRD patterns of MnOOH, Mn<sub>3</sub>O<sub>4</sub>, rGO/Mn<sub>3</sub>O<sub>4</sub> and ArGO/Mn<sub>3</sub>O<sub>4</sub> NR. The diffraction peaks of MnOOH NRs can be indexed to a mixture of  $\gamma$ -MnOOH and Mn<sub>3</sub>O<sub>4</sub>. The results indicate that MnOOH NR is comprised of predominant  $\gamma$ -MnOOH and some Mn<sub>3</sub>O<sub>4</sub>. In the case of Mn<sub>3</sub>O<sub>4</sub> NR, it consists of two phases as Mn<sub>3</sub>O<sub>4</sub> and Mn<sub>5</sub>O<sub>8</sub> indicating that the only MnOOH NR without GO or AGO is not completely reduced to Mn<sub>3</sub>O<sub>4</sub> NR. On the other hand, the XRD peaks of rGO/Mn<sub>3</sub>O<sub>4</sub> and ArGO/Mn<sub>3</sub>O<sub>4</sub> nanocomposites match well to Mn<sub>3</sub>O<sub>4</sub> Hausmannite (JCPDS No. 24-0734). The diffraction peaks at 18.0°, 28.9°, 31.0°, 32.3°, 36.1° and 38.1° can be assigned to (101), (112), (200), (103), (211) and (004) planes of the tetragonal Mn<sub>3</sub>O<sub>4</sub>. As observed, the peaks of rGO and ArGO is not distinguished due to a lower content and intensity than those of Mn<sub>3</sub>O<sub>4</sub> NRs. It can be reasonably deduced from the results that MnOOH NRs including GO and AGO is more completely transformed to Mn<sub>3</sub>O<sub>4</sub> NRs.

**Figure 30** presents the nitrogen adsorption/desorption isotherms and pore-size distribution of Mn<sub>3</sub>O<sub>4</sub>, rGO/Mn<sub>3</sub>O<sub>4</sub> and ArGO/Mn<sub>3</sub>O<sub>4</sub> NR.

As shown in **Figure 30a**, the isotherm of the ArGO/Mn<sub>3</sub>O<sub>4</sub> NR nanocomposite was classified as type IV with an H3 hysteresis loop. ArGO/Mn<sub>3</sub>O<sub>4</sub> NR exhibits a higher SSA than bare Mn<sub>3</sub>O<sub>4</sub> and rGO/Mn<sub>3</sub>O<sub>4</sub> NR because of the restrained aggregation of the nanorods and the introduction of acid-treated graphene nanosheet with a relatively large SSA. According to BJH data, the pore-size distribution and pore volume for ArGO/Mn<sub>3</sub>O<sub>4</sub> NR are much higher than those for bare Mn<sub>3</sub>O<sub>4</sub> and rGO/Mn<sub>3</sub>O<sub>4</sub> NR. It is believed that ArGO is contributed to SSA and pore volume.

**Figure 31** displays SEM images of MnOOH, Mn<sub>3</sub>O<sub>4</sub>, rGO/Mn<sub>3</sub>O<sub>4</sub> and ArGO/Mn<sub>3</sub>O<sub>4</sub> NR. It demonstrates that MnOOH NRs were transformed to Mn<sub>3</sub>O<sub>4</sub> NRs without any deformation during heat treatment. After AGO (or GO) and MnOOH NRs were reduced, a ArGO (or rGO)/Mn<sub>3</sub>O<sub>4</sub> sandwich-like structure was finally formed due to the restacking of the hydrophobic graphene nanosheet in **Figure 31c-f**. This sandwich-like structure acts as a strain buffer for the volume change of Mn<sub>3</sub>O<sub>4</sub> NRs during the electrochemical reaction. In addition, the 1D structure of the nanorods provides a short diffusion length for Li ion and electron transport along the 1D direction. Through the transparent rGO and ArGO, it is clear that Mn<sub>3</sub>O<sub>4</sub> NRs

are confined inbetween graphene nanosheets, which provide the pathway and open channel for Li ions and electrons, respectively. A large contact interface between electrode and electrolyte is also formed in this structure. Furthermore, **Figure 31c-f** clearly indicates that  $\text{Mn}_3\text{O}_4$  NRs in the nanocomposite are uniformly distributed and continuously interconnected with rGO and ArGO. As a consequence of the ArGO (rGO)/ $\text{Mn}_3\text{O}_4$  NR structure, it is anticipated that the electrolyte wettability over the entire nanocomposite and an effective diffusion for lithium ions and electrons is favorable. The morphology of the ArGO/ $\text{Mn}_3\text{O}_4$  NR after 100 cycles was also characterized by SEM as shown in **Figure 32**.  $\text{Mn}_3\text{O}_4$  NRs still retain their 1D structure and SEI around them is observed. It confirms that ArGO nanosheets function as buffer layers to prevent the volume change of  $\text{Mn}_3\text{O}_4$  NRs.

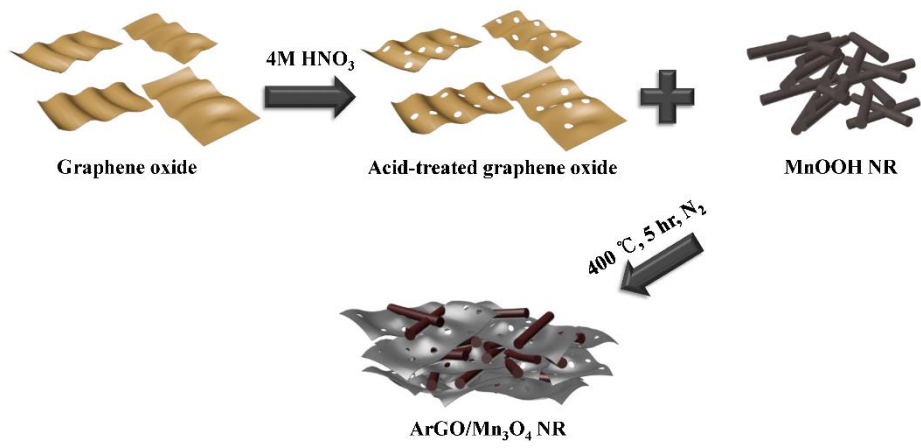


**Figure 28** Schematic preparation of nanocomposite.

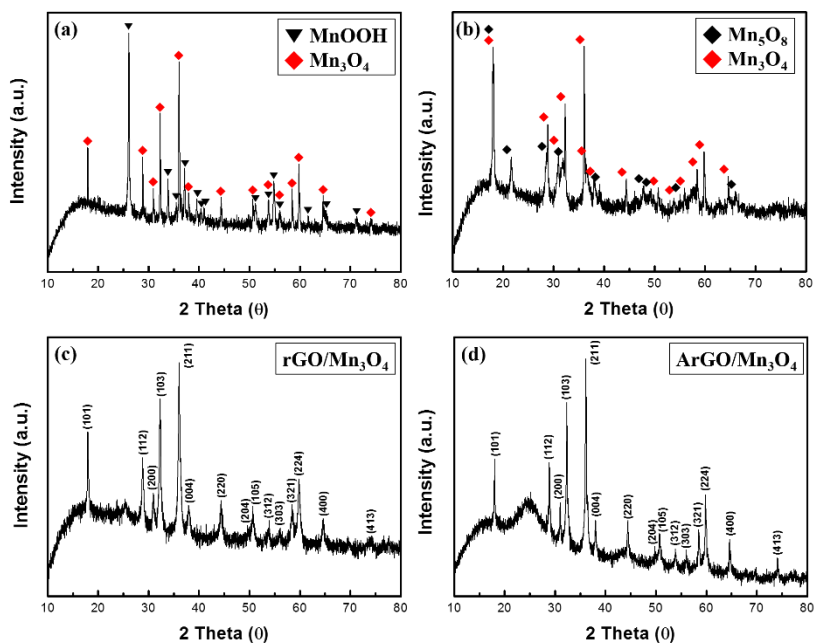


**Figure 29** XRD patterns of (a)  $\text{MnOOH}$  NR, (b)  $\text{Mn}_3\text{O}_4$  NR, (c)  $\text{rGO}/\text{Mn}_3\text{O}_4$  and (d)  $\text{ArGO}/\text{Mn}_3\text{O}_4$ .

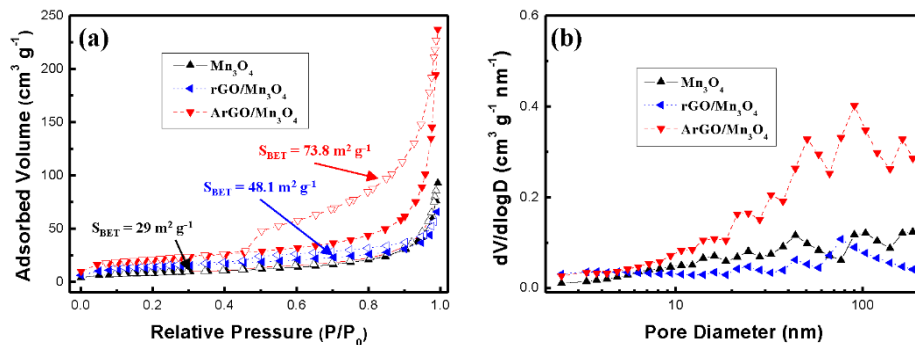


**Figure 30** (a) Nitrogen adsorption/desorption isotherms and (b) pore-size distribution of  $\text{Mn}_3\text{O}_4$  NR,  $\text{rGO}/\text{Mn}_3\text{O}_4$  and  $\text{ArGO}/\text{Mn}_3\text{O}_4$ .

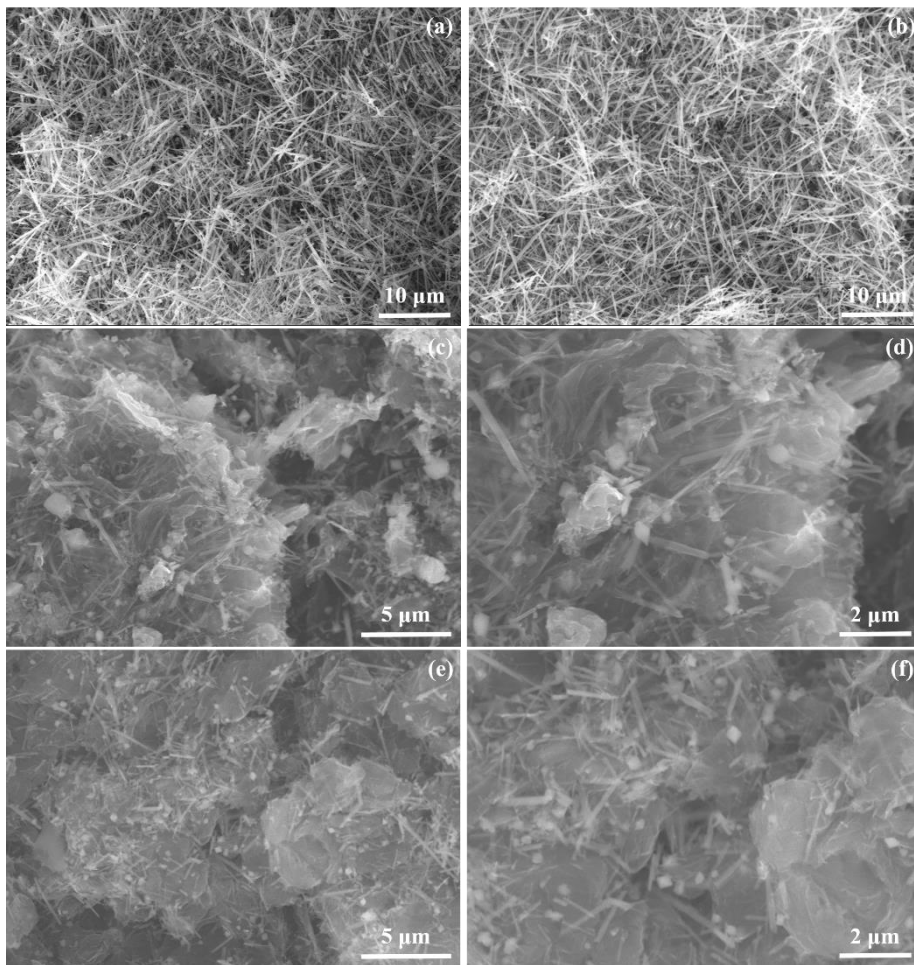


**Figure 31** SEM images of (a) MnOOH, (b) Mn<sub>3</sub>O<sub>4</sub>, (c, d) rGO/Mn<sub>3</sub>O<sub>4</sub> and (e, f) ArGO/Mn<sub>3</sub>O<sub>4</sub> NR.

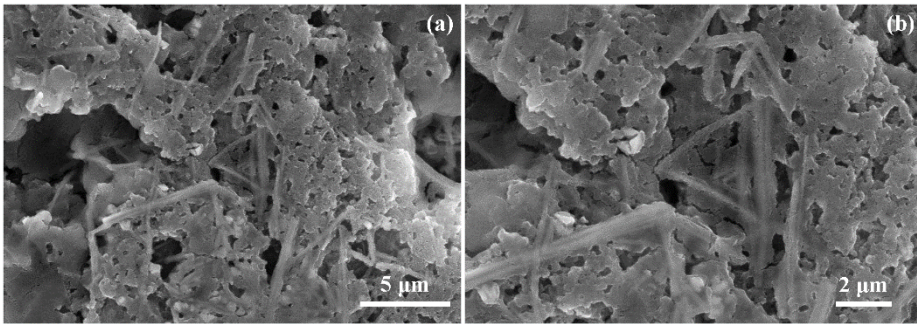


**Figure 32** SEM images of the ArGO/Mn<sub>3</sub>O<sub>4</sub> NR after 100 cycles.

The crystalline structure and morphology of  $\text{Mn}_3\text{O}_4$ ,  $\text{rGO}/\text{Mn}_3\text{O}_4$  and  $\text{ArGO}/\text{Mn}_3\text{O}_4$  NR were further studied by TEM and HR-TEM, as shown in **Figure 33**. Without any structural variation,  $\text{Mn}_3\text{O}_4$  NRs (**Figure 33a**) were formed after heat treatment, which is well matched with SEM results (**Figure 33a and b**). In HR-TEM image of  $\text{rGO}/\text{Mn}_3\text{O}_4$  and  $\text{ArGO}/\text{Mn}_3\text{O}_4$  NR (the inset of **Figure 33b and d**),  $\text{Mn}_3\text{O}_4$  NRs clearly have crystal lattice fringes of 0.31 and 0.27 nm, corresponding to the (112) and (103) planes, respectively.

Cyclic voltammetry (CV) tests were performed at a scan rate of 0.1  $\text{mV s}^{-1}$  between 0.01 and 3 V to understand the redox reactions to  $\text{Mn}_3\text{O}_4$  NR,  $\text{rGO}/\text{Mn}_3\text{O}_4$  NR and  $\text{ArGO}/\text{Mn}_3\text{O}_4$  NR as anode materials. The 1<sup>st</sup>, 2<sup>nd</sup>, 5<sup>th</sup> and 10<sup>th</sup> of CV curves for all electrodes are presented in the **Figure 34a, c and e**. In the first cycle of the  $\text{Mn}_3\text{O}_4$  NR electrode, a broad cathodic peak in the range of 0.5-1.9 V was observed and disappeared in the following cycles, which is ascribed to the formation of SEI due to the electrolyte decomposition and the reduction of  $\text{Mn}_3\text{O}_4$  ( $\text{Mn}^{3+}$ ) to  $\text{MnO}$  ( $\text{Mn}^{2+}$ ). In addition, the strong cathodic peak centered at 0.035 V is attributed to the reduction of  $\text{MnO}$  ( $\text{Mn}^{2+}$ ) to  $\text{Mn}$  ( $\text{Mn}^0$ ). After the first cycle, the reduction peak shifts from 0.035 to ca. 0.35 V because of the structural

transformations during the first discharge. The anodic peak at 1.3 V corresponds to the oxidation of Mn to MnO. For the Mn<sub>3</sub>O<sub>4</sub> NR electrode, this peak intensity decreases drastically which means the poor reversibility. As shown in the **Figure 34c**, the CV curve for the rGO/Mn<sub>3</sub>O<sub>4</sub> NR demonstrates the effect of reduced graphene oxides when Mn<sub>3</sub>O<sub>4</sub> NRs are mixed with rGO. Unlike the Mn<sub>3</sub>O<sub>4</sub> electrode, the reversible capacity of the rGO/Mn<sub>3</sub>O<sub>4</sub> NR electrode is pronouncedly enhanced. In the case of the ArGO/Mn<sub>3</sub>O<sub>4</sub> NR electrode, there is another anodic peak at 2.34 V which is related with the further oxidation of MnO to Mn<sub>3</sub>O<sub>4</sub>. Furthermore, the cathodic peak at 1.65 V is clearly observed and associated with the reduction of Mn<sub>3</sub>O<sub>4</sub> to MnO. It is anticipated that lithium ions may easily pass through graphene sheets without detouring. As a result of the CV curves, ArGO/Mn<sub>3</sub>O<sub>4</sub> NR electrode displays a higher reversible capacity than Mn<sub>3</sub>O<sub>4</sub> and rGO/Mn<sub>3</sub>O<sub>4</sub> NR electrodes. Based on the CV analyses and the previous studies, the mechanism for the electrochemical conversion reaction between Li and Mn<sub>3</sub>O<sub>4</sub> can be expressed by the following equation:

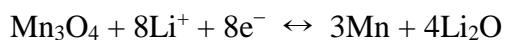


**Figure 34b, d and f** shows the 1<sup>st</sup>, 2<sup>nd</sup>, 5<sup>th</sup> and 10<sup>th</sup> charge-discharge curves for all electrodes at a current density of 200 mA g<sup>-1</sup> between 0.01 and 3 V. The curves are well-matched with the previous reports on the charge-discharge trend of Mn<sub>3</sub>O<sub>4</sub> anodes. During the first discharge, the voltage plateau at 1.25 V is sloping down to 0.27 V, which is mainly attributed to the SEI formation and the initial reduction of Mn<sub>3</sub>O<sub>4</sub> to MnO. The long voltage plateau from 0.27 V to 0.01 V indicates that MnO is further reduced to Mn. After the first cycle, the plateau at 0.27 V moves up to 0.45 V, which implies that lithium ions can readily react with MnO in the following cycles. On the other hand, the voltage plateau at 1.25 V results from the oxidation of Mn to MnO while the electrodes are charging.

Mn<sub>3</sub>O<sub>4</sub>, rGO/Mn<sub>3</sub>O<sub>4</sub> and ArGO/Mn<sub>3</sub>O<sub>4</sub> NR electrodes deliver a first discharge capacity of 1060, 1100 and 1130 mA h g<sup>-1</sup> and then a reversible capacity of 556, 695 and 778 mA h g<sup>-1</sup>, respectively. The ArGO/Mn<sub>3</sub>O<sub>4</sub> NR electrode exhibits a lower initial irreversible capacity of 32% than those of 48 and 37% for Mn<sub>3</sub>O<sub>4</sub> and rGO/Mn<sub>3</sub>O<sub>4</sub> NR electrodes, respectively. The capacity loss for the first cycle is mainly due to the SEI formation by the decomposition of electrolyte and the large volume change which is the common phenomenon

relating to the conversion reaction for anode materials. Coulombic efficiency increases to 98% after 3 cycles. The reversible capacity reaches to 749 mA h g<sup>-1</sup> after 100 cycles, higher than other anode materials.

Among all electrodes, the ArGO/Mn<sub>3</sub>O<sub>4</sub> NR electrode presents the most excellent reversibility because acid-treated reduced graphene oxides have the performance of the electrode improved. Consequently, the ArGO/Mn<sub>3</sub>O<sub>4</sub> NR electrode has more stable and reversible charge-discharge process than other electrodes due to acid treatment of graphene oxide, which may promote the transportation for lithium ions and electrons through ArGO sheets.

The cycle performance tests of electrodes were performed at a current density of 200 mA g<sup>-1</sup> and the results were given in **Figure 35a**. The initial charge capacity is 778 mAh g<sup>-1</sup>, and thereafter, the capacity decreases gradually. However, it is interesting that a gradual increase of capacity is also observed after the capacity reaches a minimum capacity. A high capacity of 749 mAh g<sup>-1</sup> is achieved after 100 cycles. This capacity variation has been reported on many transitional metal oxides, particularly nanostructured Mn<sub>x</sub>O<sub>y</sub>. Lowe and co-workers proposed that the extra capacity may be contributed to

a capacitive-like charge storage. Yonekura et al. suggested that the increasing capacity was caused by the degradation of electrolyte. This phenomenon, proposed by J. M. Tarascon, might be related to the reversible growth of a polymeric gel-like film catalyzed by 3d metals. The capacity increase that comes from activation of electrode materials could be another possibility. In other words, small nanoparticles not only increase the surface area but also active sites for lithium storage. The polymeric gel-like SEI layer which can improve the mechanical cohesion among the active materials without hindering the ion transfer is formed by the electrolyte decomposition.

The rate performance of bare  $\text{Mn}_3\text{O}_4$ ,  $\text{rGO}/\text{Mn}_3\text{O}_4$  and  $\text{ArGO}/\text{Mn}_3\text{O}_4$  NR nanocomposites from 100 to 2000  $\text{mA g}^{-1}$  is shown in **Figure 35b**. The  $\text{ArGO}/\text{Mn}_3\text{O}_4$  electrode delivers a high capacity of 948, 778, 597, 509, and 412  $\text{mA}\cdot\text{h}\cdot\text{g}^{-1}$  at different current densities of 100, 200, 500, 1000, and 2000  $\text{mA}\cdot\text{g}^{-1}$ , respectively. When the current density returned to 100  $\text{mA}\cdot\text{g}^{-1}$ , the discharge capacity of the  $\text{ArGO}/\text{Mn}_3\text{O}_4$  electrode remarkably recovered to 802  $\text{mA}\cdot\text{h}\cdot\text{g}^{-1}$ . This performance presents that a high current density doesn't affect the  $\text{ArGO}/\text{Mn}_3\text{O}_4$  NR electrode.

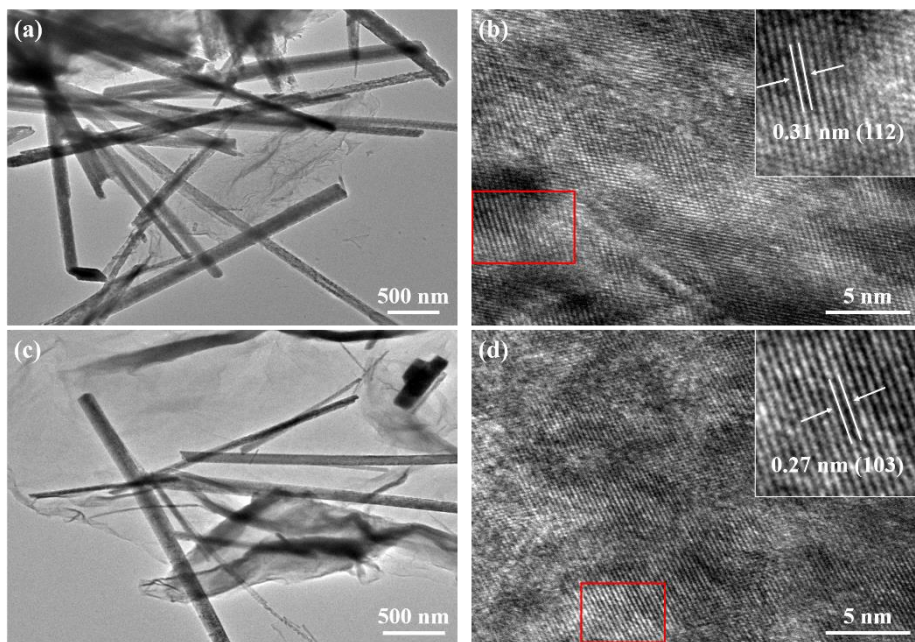


**Figure 33** TEM and HR-TEM images of (a, b) rGO/Mn<sub>3</sub>O<sub>4</sub> and (c, d) ArGO/Mn<sub>3</sub>O<sub>4</sub> NR.

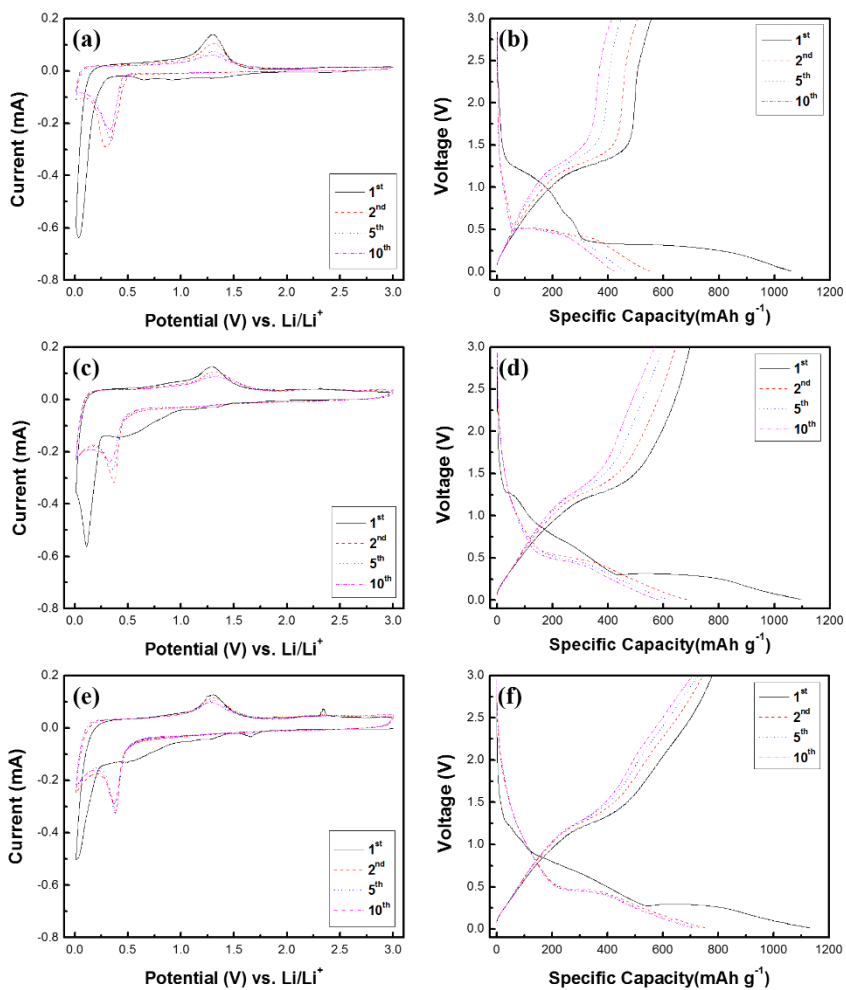


**Figure 34** Cyclic voltammograms and charge–discharge profiles of (a, b)  $\text{Mn}_3\text{O}_4$ , (c, d)  $\text{rGO}/\text{Mn}_3\text{O}_4$  and (e, f)  $\text{ArGO}/\text{Mn}_3\text{O}_4$  NR.

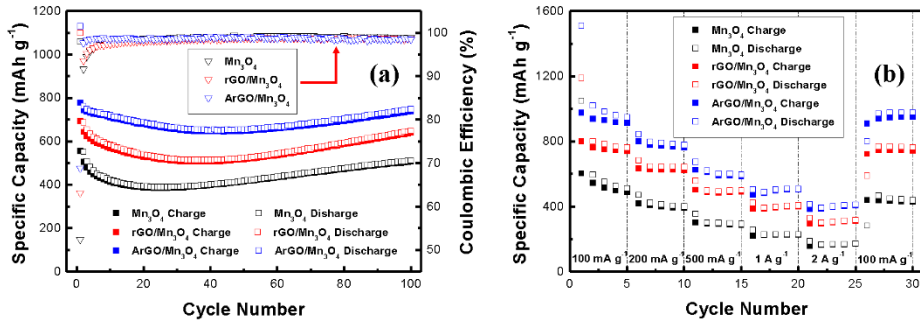


**Figure 35** Comparative cycle performance of  $\text{Mn}_3\text{O}_4$  NR,  $\text{rGO}/\text{Mn}_3\text{O}_4$  NR and  $\text{ArGO}/\text{Mn}_3\text{O}_4$  NR at a current density of 200  $\text{mA g}^{-1}$  (a) and rate capability of  $\text{Mn}_3\text{O}_4$  NR,  $\text{rGO}/\text{Mn}_3\text{O}_4$  NR and  $\text{ArGO}/\text{Mn}_3\text{O}_4$  NR at various current densities (b).

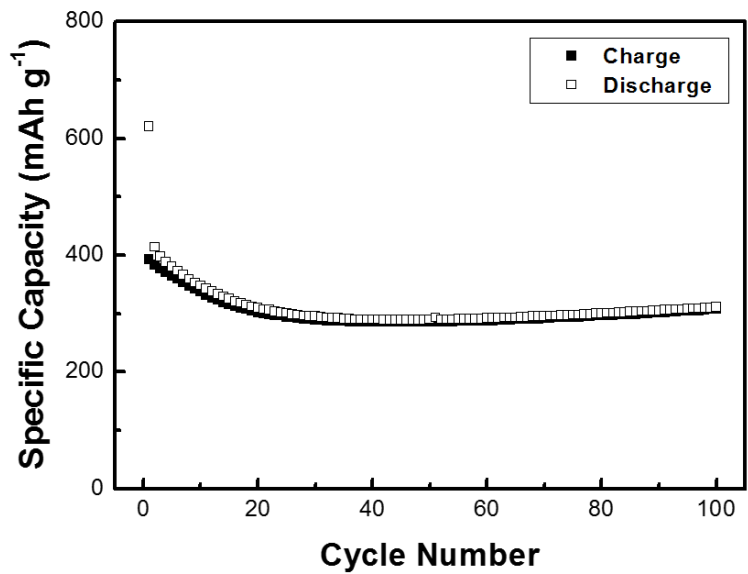


**Figure 36** Cycle performance of ArGO at a current density of 200 mA g<sup>-1</sup>.

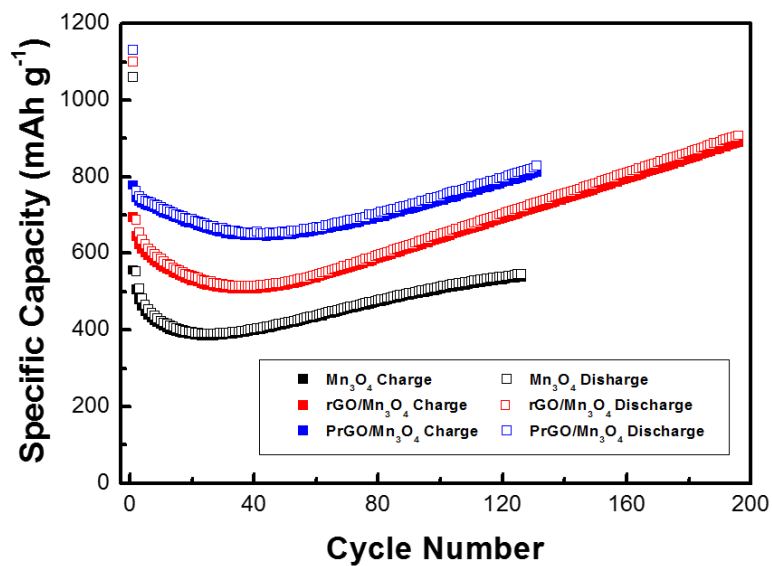


**Figure 37** Comparative cycle performance of Mn<sub>3</sub>O<sub>4</sub> NR, rGO/Mn<sub>3</sub>O<sub>4</sub> NR and ArGO/Mn<sub>3</sub>O<sub>4</sub> NR.

### **4.3. An Acid-treated Reduced Graphene Oxide/Tin Oxide Nanocomposite as an Anode Material for Lithium Ion Batteries**

In the **Figure 39**, the X-ray diffraction patterns demonstrate the structural characteristic of SnO<sub>2</sub>, GS, AGS. The XRD patterns of SnO<sub>2</sub>, GS and AGS exhibit four major diffraction peaks (110), (101), (200), and (211) planes of the tetragonal rutile SnO<sub>2</sub> phase, which is consistent with 0.335, 0.264, 0.236 and 0.176 nm d-spacing (Cassiterite, JCPDS card No. 41-1445). These peaks are so broad that they signify a small particle size of SnO<sub>2</sub>. The average crystallite size through Scherrer's formula is 3.7 nm, well matched with the TEM results. However, it is unable to discriminate the peaks of rGO or ArGO from those of GS or AGS due to a lower content and intensity than those of SnO<sub>2</sub>.

The morphology and crystalline structure of GS and AGS loaded on graphene are further examined by SEM, low-magnification and high-resolution TEM. In SEM images of **Figure 40**, SnO<sub>2</sub> nanoparticles are not clearly distinguished from graphene because of the small particle size. Despite that, it is presumed that there are nanoparticles on graphene with the rough surface. On the other hand, it is clear that SnO<sub>2</sub> nanoparticles are uniformly synthesized and deposited on graphene in **Figure 41**. From the TEM results, SnO<sub>2</sub> nanoparticles

ranging from 3 to 5 nm as shown in **Figure 42a and c** are homogeneously dispersed on the graphene surface. **Figure 42b and d** reveal clear lattice fringes with a spacing of 0.32 and 0.24 nm, corresponding to the (110) and (200). The elemental mapping analysis in **Figure 43** reveals that AGS is mainly composed of carbon, tin and oxygen, spreading identically throughout the graphene surface.

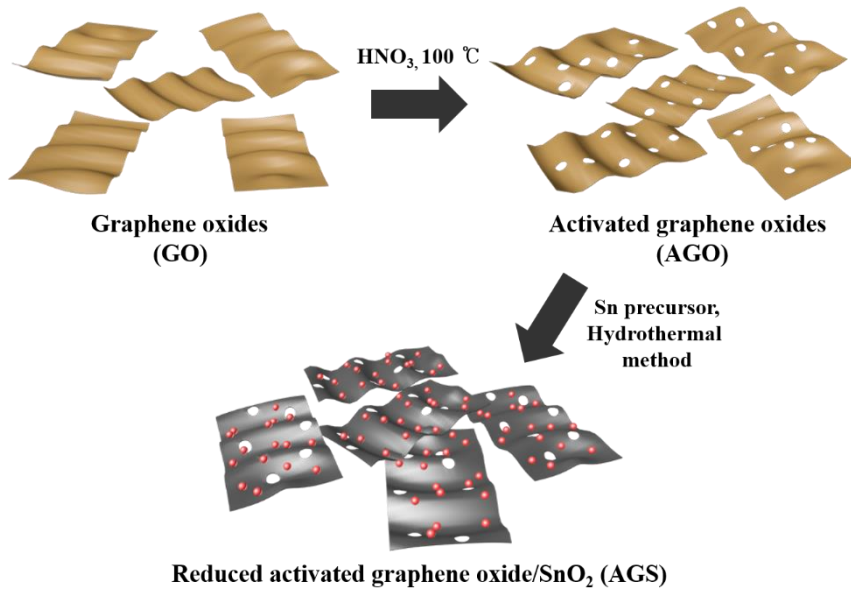


**Figure 38** Schematic diagram for preparation of the nanocomposite.

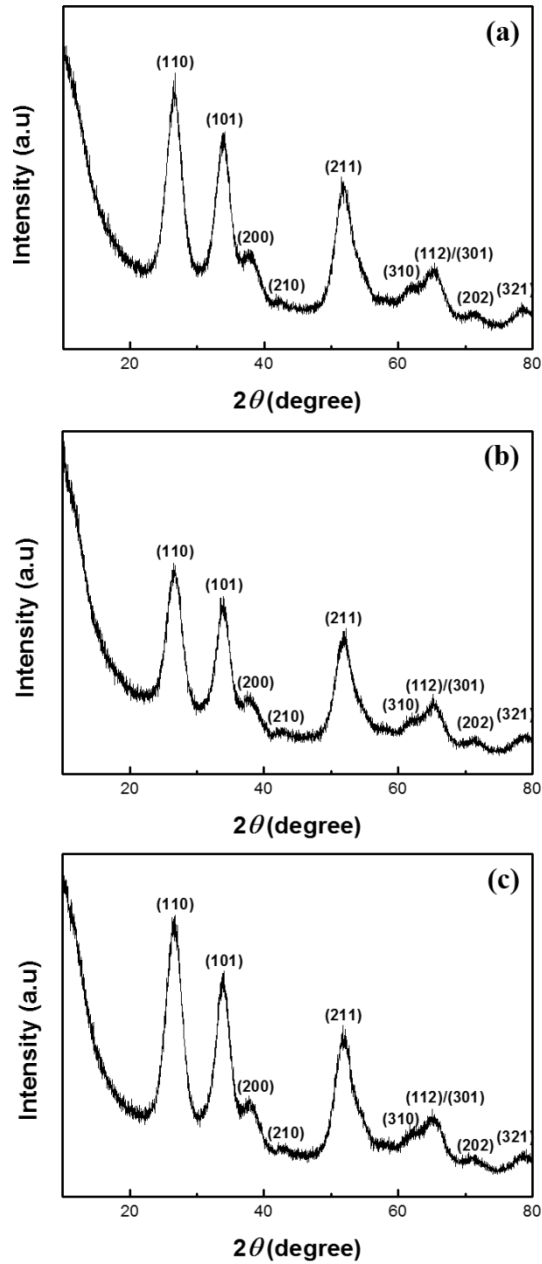


**Figure 39** X-ray diffraction patterns of SnO<sub>2</sub>, GS and AGS (a, b and c).

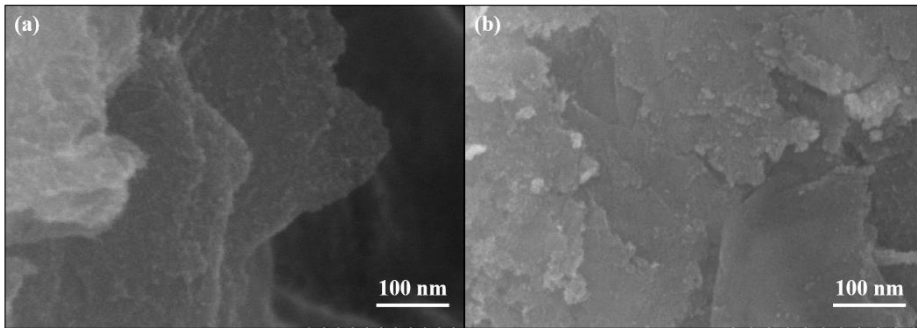


**Figure 40** SEM images of AGS (a) and GS (b).

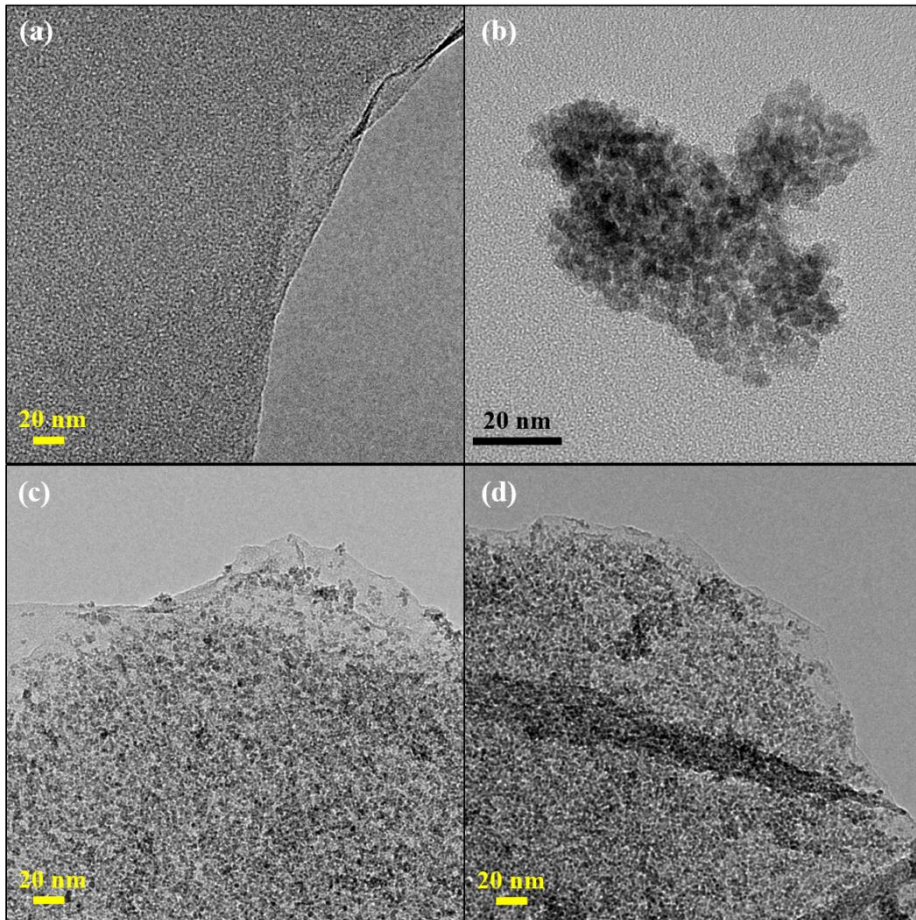


**Figure 41** TEM images of ArGO (a), SnO<sub>2</sub> (b), GS (c) and AGS (d).

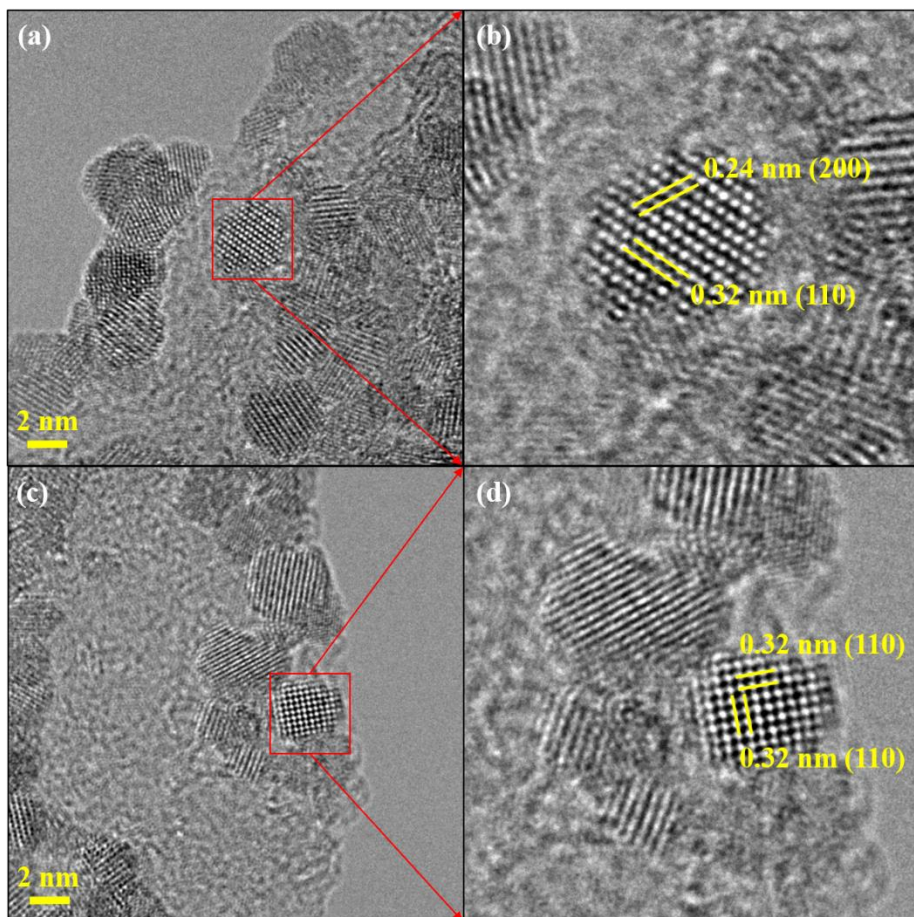


**Figure 42** HR-TEM images of GS (a and b) and AGS (c and d).

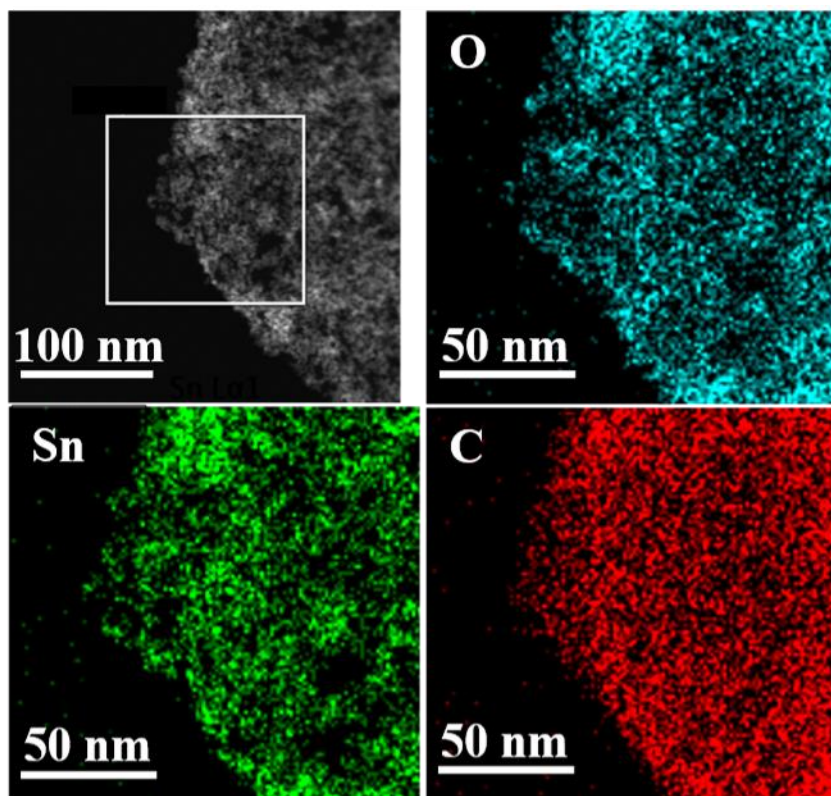
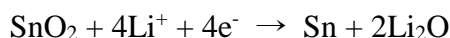


**Figure 43** Dark-field TEM image and the corresponding Sn, C, and O element mapping.

Galvanostatic charge-discharge cycling performances of SnO<sub>2</sub>, GS and AGS are evaluated between 0.01 and 2 V at a current density of 200 mA g<sup>-1</sup>. In **Figure 44a, b and c**, SnO<sub>2</sub>, GS and AGS electrodes displays a first charge and discharge capacity of 807 and 1640, 918 and 1940, 979 and 2030 mA h g<sup>-1</sup>. According to the first cycle, the coulombic efficiencies of each electrode correspond to 49, 47 and 48%, respectively. The huge capacity loss in the first cycle is due to the irreversible reduction of SnO<sub>2</sub> to Sn, amorphous Li<sub>2</sub>O and SEI layer.



After 20 cycles, the AGS electrode is more stable than other electrodes, SnO<sub>2</sub> and GS. The SnO<sub>2</sub> electrode capacity is drastically decreased in the following cycles, which results from the volume change while the AGS electrode steadily maintains its capacity without significant loss. As shown in **Figure 44d, e and f**, cyclic voltammeteries of SnO<sub>2</sub>, GS and AGS at a scan rate of 0.1 mV s<sup>-1</sup> in a voltage range of 0.01 ~ 2.0 V are presented for better understanding of the reaction

mechanism. The weak cathodic peak at around 0.74 V relating to the formation of SEI layer is irreversible and disappeared in the following cycles. The cathodic peak at around 0.12 V and the anodic peak at around 0.54V come from the lithium alloying and de-alloying reaction with Sn and  $\text{Li}_x\text{Sn}$ , respectively. Another cathodic peak at around 0.01 V and anodic peak at around 0.1 V are related to the lithium insertion/extraction through graphene sheets. In addition, the peak at around 1.23V is ascribed to the partly reversible conversion of Sn to  $\text{SnO}_2$ .

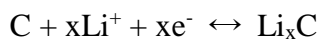


**Figure 45a and b** present the cycling performance of  $\text{SnO}_2$ , GS and AGS at different current densities, 200 and 500  $\text{mA g}^{-1}$ . In both cases, the capacity for the bare  $\text{SnO}_2$  electrode diminishes more rapidly than the others due to the repetitive volume expansion and contraction during the cycling, resulting in the aggregation of Sn. For GS and AGS, graphene plays an important role in avoiding aggregation of Sn metal

nanoparticles into larger clusters. Therefore, GS and AGS electrodes show much better cyclability than the bare SnO<sub>2</sub> electrode. Especially, the AGS electrode delivers the highest capacity even at a high current density owing to the existence of ArGO, which accommodates the volume expansion and provides the pathway for Li ions and electrons.

**Figure 45c** indicates the rate performance of SnO<sub>2</sub>, GS and AGS evaluated at various current densities, 0.1, 0.2, 0.5, 1, 2 and 5 A. It elucidates a point of importance for the graphene framework, which makes the electron transfer and the stability of the electrode improved. Even at a current density of 5 A g<sup>-1</sup>, AGS delivered a higher capacity of 520 mA h g<sup>-1</sup>, which is still higher than commercially available graphite (372 mA h g<sup>-1</sup>), than SnO<sub>2</sub> and GS of 50 and 330 mA h g<sup>-1</sup>.

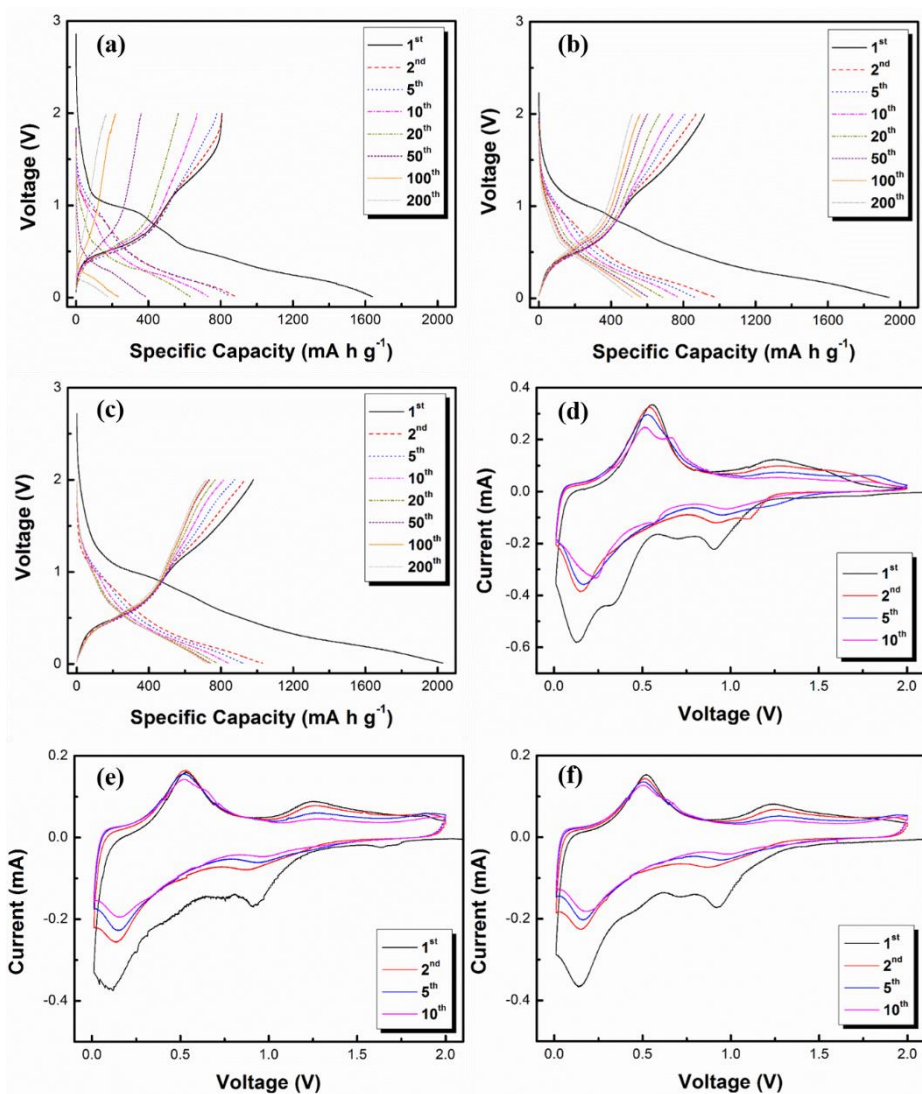


**Figure 44** Galvanostatic charge–discharge profiles of SnO<sub>2</sub>, GS and AGS at 200 mA g<sup>-1</sup> (a, b and c), respectively. Cyclic voltammetry curves of SnO<sub>2</sub>, GS and AGS (d, e and f).

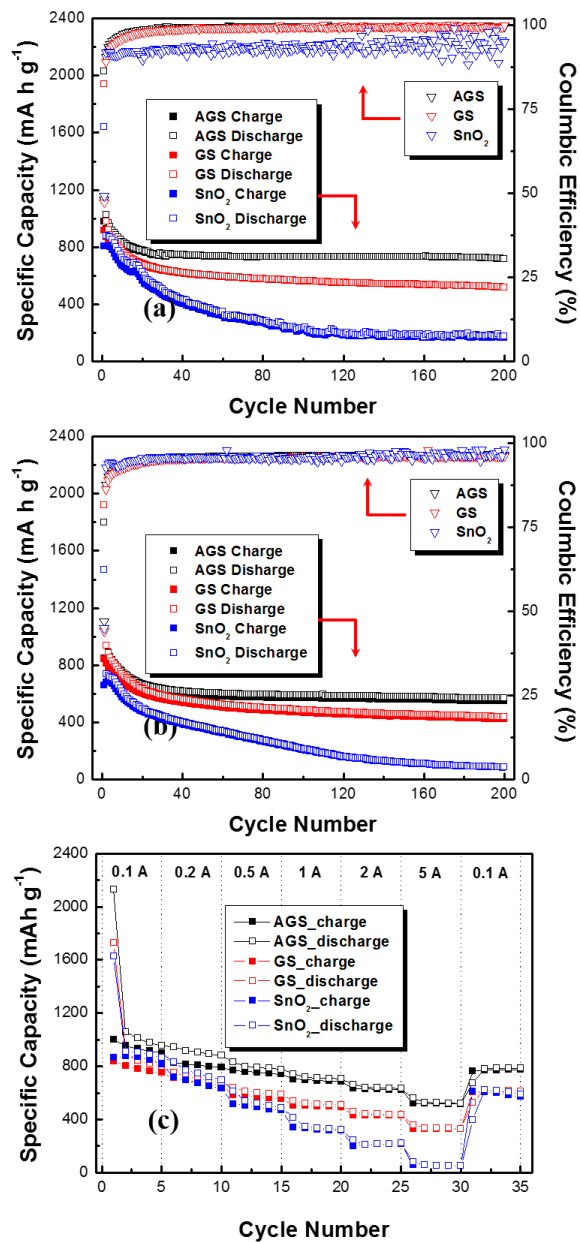


**Figure 45** Cycling performance at 200 mA g<sup>-1</sup> and 500 mA g<sup>-1</sup> (a and b) and rate performances of SnO<sub>2</sub>, GS and AGS at different current densities (c).

## **Chapter 5. Conclusion**

In this dissertation, various hybrid nanocomposites were developed by a variety of methods, such as vacuum filtration, hydrothermal synthesis and simple mixing process, based on reduced graphene oxide which consists of single atom of carbon. The graphene-based nanocomposites were used as anode electrodes due to their remarkable electrochemical and mechanical properties. These nanocomposites have been expected to be promising candidates for next-generation electrodes with high energy density and stability.

This dissertation covered graphene-based anode nanomaterials relating to graphene paper, metal oxide/graphene composite and metal oxide on graphene in LIBs. Firstly, the  $\text{Mn}_3\text{O}_4$  nanorods/reduced graphene oxide paper, which is hierarchically stacked, fabricated by vacuum filtration process and applied to an anode electrode in LIBs showed the first discharge and charge capacities of 943 and 627  $\text{mA}\cdot\text{h}\cdot\text{g}^{-1}$ , respectively and Coulombic efficiency of 66.5%. It is ascribed to reduce graphene oxide paper, which plays a decisive role in alleviating the volume expansion of  $\text{Mn}_3\text{O}_4$  nanorods when lithium ions are inserted and extracted and enhancing Li ion and electron transport.  $\text{Mn}_3\text{O}_4$  nanorod provides the efficient pathway for electrons and Li ions as well. In addition, the out-of-plane porous structure leads to facile lithium

transfer. The porous  $\text{Mn}_3\text{O}_4$  nanorod/reduced graphene oxide paper delivered  $573 \text{ mA}\cdot\text{h}\cdot\text{g}^{-1}$  even in 100 cycles when compared to a bare reduced graphene oxide paper. The porous  $\text{Mn}_3\text{O}_4$  nanorod/reduced graphene oxide at 50, 100, 500, 1000, and 2000  $\text{mA g}^{-1}$  also delivered 692, 618, 411, 313, and 196  $\text{mA h g}^{-1}$ , respectively. Consequently, the porous  $\text{Mn}_3\text{O}_4$  nanorod/reduced graphene oxide paper showed the high reversible capacity, stable cyclability and better rate capability.

Secondly, to produce pores on the surface, graphene oxide was treated by nitric acid. The acid-treated reduced graphene oxide not only provides Li ion transport through pores but electron transport over the whole surface and pores.  $\text{Mn}_3\text{O}_4$  nanorods, which has a one-dimensional structure, have a large contact area between electrolyte and nanorod and provide efficient electron transport along nanorods and short Li ion diffusion length. Furthermore, the acid-treated reduced graphene oxide/ $\text{Mn}_3\text{O}_4$  nanorod was prepared by simple mixing and reduction process. This electrode delivered 1130 and 778  $\text{mA}\cdot\text{h}\cdot\text{g}^{-1}$  at 200  $\text{mA}\cdot\text{g}^{-1}$  during the first charge and discharge, respectively. The overall capacity of the electrode reached to 749  $\text{mA}\cdot\text{h}\cdot\text{g}^{-1}$  after 100 cycles.

Finally,  $\text{SnO}_2$  nanoparticles were hydrothermally deposited onto

graphene surface. To render in-plane pores on graphite oxide, graphite was oxidized by oxidants and then activated by nitric acid. Through reduction, the acid-treated reduced graphene oxide acts as a host material and buffer layer for SnO<sub>2</sub> to avoid suffering from pulverization and volume change while Li<sup>+</sup> is alloyed into and dealloyed from SnO<sub>2</sub>. Moreover, Li ion and electron transfer are expected to be improved by the acid-treated reduced graphene oxide, leading to better rate capability. As a result, the acid-treated reduced graphene oxide/SnO<sub>2</sub> anode presented the first charge and discharge capacity of 979 and 2030 mA h g<sup>-1</sup>. Additionally, the acid-treated reduced graphene oxide/SnO<sub>2</sub> anode maintains 720 and 569 mA h g<sup>-1</sup> at 200 and 500 mA g<sup>-1</sup>, respectively after 200 cycles.

In the dissertation, it implies that various graphene-based nanocomposites can help anode electrodes have high capacity, better rate capability and stable cyclability and so on in lithium ion batteries. Therefore, it is hopefully expected that these nanomaterials have a great potential to be energy storage materials for lithium ion batteries.

## References

- [1] M. S. Whittingham, *Chem. Rev.*, 2004, 104, 4271.
- [2] M. Armand and J. M. Tarascon, *Nature*, 2008, 451, 652.
- [3] J. M. Tarascon and M. Armand, *Nature*, 2001, 414, 359.
- [4] P. G. Bruce, B. Scrosati and J. M. Tarascon, *Angew. Chem. Int. Ed. Engl.*, 2008, 47, 2930.
- [5] S. Goriparti, E. Miele, F. De Angelis, E. Di Fabrizio, R. Proietti Zaccaria and C. Capiglia, *J. Power Sources*, 2014, 257, 421.
- [6] B. Dunn, H. Kamath and J. M. Tarascon, *Science*, 2011, 334, 928.
- [7] N. S. Choi, Z. Chen, S. A. Freunberger, X. Ji, Y. K. Sun, K. Amine, G. Yushin, L. F. Nazar, J. Cho and P. G. Bruce, *Angew. Chem. Int. Ed. Engl.*, 2012, 51, 9994.
- [8] M. G. Kim and J. Cho, *Adv. Funct. Mater.*, 2009, 19, 1497.
- [9] Y. Li, B. Tan and Y. Wu, *Nano Lett.*, 2008, 8, 265.
- [10] Y. Lu, Y. Wang, Y. Zou, Z. Jiao, B. Zhao, Y. He and M. Wu, *Electrochem. Commun.*, 2010, 12, 101.
- [11] M. Y. Son, J. H. Kim and Y. C. Kang, *Electrochim. Acta*, 2014, 116, 44.
- [12] Y. Sun, X.-Y. Feng and C.-H. Chen, *J. Power Sources*, 2011, 196, 784.

- [13] X. Yang, Y. Yang, H. Hou, Y. Zhang, L. Fang, J. Chen and X. Ji, *J. Phys. Chem. C.*, 2015, 119, 3923.
- [14] W. Zhang and D. Liu, *Electrochim. Acta*, 2015, 156, 53.
- [15] H. Jang, S. Suzuki and M. Miyayama, *J. Eur. Ceram. Soc.*, 2014, 34, 4297.
- [16] J. Yue, X. Gu, L. Chen, N. Wang, X. Jiang, H. Xu, J. Yang and Y. Qian, *J. Mater. Chem. A*, 2014, 2, 17421.
- [17] H. L. Wang, L. F. Cui, Y. A. Yang, H. S. Casalongue, J. T. Robinson, Y. Y. Liang, Y. Cui and H. J. Dai, *J. Am. Chem. Soc.*, 2010, 132, 13978.
- [18] I. Nam, N. D. Kim, G.-P. Kim, J. Park and J. Yi, *J. Power Sources*, 2013, 244, 56.
- [19] Z. Bai, X. Zhang, Y. Zhang, C. Guo and B. Tang, *J. Mater. Chem. A*, 2014, 2, 16755.
- [20] D. K. Kim, P. Muralidharan, H.-W. Lee, R. Ruffo, Y. Yang, C. K. Chan, H. Peng, R. A. Huggins and Y. Cui, *Nano Lett.*, 2008, 8, 3948.
- [21] J. Wang, N. Du, H. Wu, H. Zhang, J. Yu and D. Yang, *J. Power Sources*, 2013, 222, 32.
- [22] J. Gao, M. A. Lowe and H. c. D. Abruña, *Chem. Mater.*, 2011, 23,

3223.

- [23] A. Ponrouch, P.-L. Taberna, P. Simon and M. R. Palacín, *Electrochim. Acta*, 2012, 61, 13.
- [24] D. Pasero, N. Reeves and A. West, *J. Power Sources*, 2005, 141, 156.
- [25] Q. Fan and M. S. Whittingham, *Electrochem. Solid-State Lett.*, 2007, 10, A48.
- [26] P. Lian, J. Wang, D. Cai, L. Ding, Q. Jia and H. Wang, *Electrochim. Acta*, 2014, 116, 103.
- [27] Z. Liu, Z. Cao, B. Deng, Y. Wang, J. Shao, P. Kumar, C. R. Liu, B. Wei and G. J. Cheng, *Nanoscale*, 2014, 6, 5853.
- [28] J. Zhu, G. Zhang, X. Yu, Q. Li, B. Lu and Z. Xu, *Nano Energy*, 2014, 3, 80.
- [29] X. W. Lou, Y. Wang, C. Yuan, J. Y. Lee and L. A. Archer, *Adv. Mater.*, 2006, 18, 2325.
- [30] I. A. Courtney and J. R. Dahn, *J. Electrochem. Soc.*, 1997, 144, 2045.
- [31] X. Zhou, L. J. Wan and Y. G. Guo, *Adv. Mater.*, 2013, 25, 2152.
- [32] X. Wang, X. Cao, L. Bourgeois, H. Guan, S. Chen, Y. Zhong, D.-M. Tang, H. Li, T. Zhai, L. Li, Y. Bando and D. Golberg, *Adv.*

*Funct. Mater.*, 2012, 22, 2682.

- [33] Y.-J. Kim, H. Lee and H.-J. Sohn, *Electrochem. Commun.*, 2009, 11, 2125.
- [34] Y. Idota, T. Kubota, A. Matsufuji, Y. Maekawa and T. Miyasaka, *Science*, 1997, 276.
- [35] Z. S. Wu, G. Zhou, L. C. Yin, W. Ren, F. Li and H. M. Cheng, *Nano Energy*, 2012, 1, 107.
- [36] J. Zhu, Z. Lu, S. T. Aruna, D. Aurbach and A. Gedanken, *Chem. Mater.*, 2000, 12, 2557.
- [37] M. N. Obrovac and V. L. Chevrier, *Chem. Rev.*, 2014, 114, 11444.
- [38] D. Larcher, S. Beattie, M. Morcrette, K. Edström, J.-C. Jumas and J.-M. Tarascon, *J. Mater. Chem.*, 2007, 17, 3759.
- [39] J. Y. Huang, L. Zhong, C. M. Wang, J. P. Sullivan, W. Xu, L. Q. Zhang, S. X. Mao, N. S. Hudak, X. H. Liu, A. Subramanian, H. Fan, L. Qi, A. Kushima and J. Li, *Science*, 2010, 330, 1515.
- [40] J. Sun, L. Xiao, S. Jiang, G. Li, Y. Huang and J. Geng, *Chem. Mater.*, 2015, 27, 4594.
- [41] K. Kisu, M. Iijima, E. Iwama, M. Saito, Y. Orikasa, W. Naoi and K. Naoi, *J. Mater. Chem. A*, 2014, 2, 13058.
- [42] C. Kim, M. Noh, M. Choi, J. Cho and B. Park, *Chem. Mater.*,

2005, 17, 3297.

- [43] H. Kim, G. O. Park, Y. Kim, S. Muhammad, J. Yoo, M. Balasubramanian, Y.-H. Cho, M.-G. Kim, B. Lee, K. Kang, H. Kim, J. M. Kim and W.-S. Yoon, *Chem. Mater.*, 2014, 26, 6361.
- [44] S.-K. Park, C.-Y. Seong, S. Yoo and Y. Piao, *Energy*, 2016, 99, 266.
- [45] Z. Bai, N. Fan, Z. Ju, C. Guo, Y. Qian, B. Tang and S. Xiong, *J. Mater. Chem. A*, 2013, 1, 10985.
- [46] C. Wang, L. Yin, D. Xiang and Y. Qi, *ACS Appl. Mater. Interfaces*, 2012, 4, 1636.
- [47] S.-Y. Liu, J. Xie, Y.-X. Zheng, G.-S. Cao, T.-J. Zhu and X.-B. Zhao, *Electrochim. Acta*, 2012, 66, 271.
- [48] L. Li, Z. Guo, A. Du and H. Liu, *J. Mater. Chem.*, 2012, 22, 3600.
- [49] N. Lavoie, P. R. L. Malenfant, F. M. Courtel, Y. Abu-Lebdeh and I. J. Davidson, *J. Power Sources*, 2012, 213, 249.
- [50] Z.-H. Wang, L.-X. Yuan, Q.-G. Shao, F. Huang and Y.-H. Huang, *Mater. Lett.*, 2012, 80, 110.
- [51] S. Luo, H. Wu, Y. Wu, K. Jiang, J. Wang and S. Fan, *J. Power Sources*, 2014, 249, 463.
- [52] A. K. GEIM and K. S. NOVOSELOV, *Nat. Mater.*, 2007, 6, 183.

- [53] K. S. Novoselov, A. K. Geim, S. V. Morozov, D. Jiang, M. I. Katsnelson, I. V. Grigorieva, S. V. Dubonos and A. A. Firsov, *Nature*, 2005, 438, 197.
- [54] X. Wang, L. Jiao, K. Sheng, C. Li, L. Dai and G. Shi, *Sci. Rep.*, 2013, 3, 1996.
- [55] Z. Bai, N. Fan, Z. Ju, C. Sun and Y. Qian, *Mater. Lett.*, 2012, 76, 124.
- [56] Y. Ren, J. Wang, X. Huang, B. Yang and J. Ding, *RSC Adv.*, 2015, 5, 59208.
- [57] R. P. J. Zhu, D. P. M. D. Shaik, H. O.M, Y. Qiu and L. Zhao, *J. Electroanal. Chem.*, 2017, 794, 78.
- [58] M. S. A. Sher Shah, J. Lee, A. R. Park, Y. Choi, W.-J. Kim, J. Park, C.-H. Chung, J. Kim, B. Lim and P. J. Yoo, *Electrochim. Acta*, 2017, 224, 201.
- [59] S. Shi, T. Deng, M. Zhang and G. Yang, *Electrochim. Acta*, 2017, 246, 1104.
- [60] M.-S. Wang, Z.-Q. Wang, Z.-L. Yang, Y. Huang, J. Zheng and X. Li, *Electrochim. Acta*, 2017, 240, 7.
- [61] J. W. Long, B. Dunn, D. R. Rolison and H. S. White, *Chem. Rev.*, 2004, 104, 4463.

- [62] J. Chen and F. Cheng, *Acc. Chem. Res.*, 2009, 42, 713.
- [63] M. Winter and R. J. Brodd, *Chem. Rev.*, 2004, 104, 4245.
- [64] J. Baxter, Z. Bian, G. Chen, D. Danielson, M. S. Dresselhaus, A. G. Fedorov, T. S. Fisher, C. W. Jones, E. Maginn, U. Kortshagen, A. Manthiram, A. Nozik, D. R. Rolison, T. Sands, L. Shi, D. Sholl and Y. Wu, *Energy Environ. Sci.*, 2009, 2, 559.
- [65] A. S. Arico, P. Bruce, B. Scrosati, J. M. Tarascon and W. van Schalkwijk, *Nat. Mater.*, 2005, 4, 366.
- [66] D. Lin, Y. Liu and Y. Cui, *Nat. Nanotechnol.*, 2017, 12, 194.
- [67] L. Jaber-Ansari, H. Iddir, L. A. Curtiss and M. C. Hersam, *ACS Nano*, 2014, 8, 2399.
- [68] E. Ferg, R. J. Gummow, A. Dekock and M. M. Thackeray, *J. Electrochem. Soc.*, 1994, 141, L147.
- [69] A. N. Jansen, A. J. Kahalan, K. D. Kepler, P. A. Nelson, K. Amine, D. W. Dees, D. R. Vissers and M. M. Thackeray, *J. Power Sources*, 1999, 81, 902.
- [70] C. Xu, B. Xu, Y. Gu, Z. Xiong, J. Sun and X. S. Zhao, *Energy Environ. Sci.*, 2013, 6, 1388.
- [71] J. G. Radich and P. V. Kamat, *ACS Catal.*, 2012, 2, 807.
- [72] K. Mizushima, P. C. Jones, P. J. Wiseman and J. B. Goodenough,

- Mater. Res. Bull.*, 1980, 15, 783.
- [73] J. Xiao, D. Mei, X. Li, W. Xu, D. Wang, G. L. Graff, W. D. Bennett, Z. Nie, L. V. Saraf, I. A. Aksay, J. Liu and J. G. Zhang, *Nano Lett.*, 2011, 11, 5071.
- [74] M. Q. Zhao, X. F. Liu, Q. Zhang, G. L. Tian, J. Q. Huang, W. Zhu and F. Wei, *ACS Nano*, 2012, 6, 10759.
- [75] E. J. Yoo, J. Kim, E. Hosono, H. S. Zhou, T. Kudo and I. Honma, *Nano Lett.*, 2008, 8, 2277.
- [76] Q. Zhang, E. Uchaker, S. L. Candelaria and G. Cao, *Chem. Soc. Rev.*, 2013, 42, 3127.
- [77] B. Luo and L. Zhi, *Energy Environ. Sci.*, 2015, 8, 456.
- [78] Y. Zhu, S. Murali, W. Cai, X. Li, J. W. Suk, J. R. Potts and R. S. Ruoff, *Adv. Mater.*, 2010, 22, 3906.
- [79] S. Park and R. S. Ruoff, *Nat. Nanotechnol.*, 2009, 4, 217.
- [80] D. R. Dreyer, S. Park, C. W. Bielawski and R. S. Ruoff, *Chem. Soc. Rev.*, 2010, 39, 228.
- [81] K. S. Novoselov, V. I. Fal'ko, L. Colombo, P. R. Gellert, M. G. Schwab and K. Kim, *Nature*, 2012, 490, 192.
- [82] B. C. Brodie, *Philos. Trans. R. Soc. Lond.*, 1859, 149, 249.
- [83] A. Yu, P. Ramesh, M. E. Itkis, E. Bekyarova and R. C. Haddon, *J.*

*Phys. Chem.*, 2007, 111, 7565.

- [84] N. G. Shang, P. Papakonstantinou, M. McMullan, M. Chu, A. Stamboulis, A. Potenza, S. S. Dhesi and H. Marchetto, *Adv. Funct. Mater.*, 2008, 18, 3506.
- [85] K. S. Novoselov, A. K. Geim, S. V. Morozov, D. Jiang, Y. Zhang, S. V. Dubonos, I. V. Grigorieva and A. A. Firsov, *Science*, 2004, 306, 666.
- [86] D. V. Kosynkin, A. L. Higginbotham, A. Sinitskii, J. R. Lomeda, A. Dimiev, B. K. Price and J. M. Tour, *Nature*, 2009, 458, 872.
- [87] L. Jiao, L. Zhang, X. Wang, G. Diankov and H. Dai, *Nature*, 2009, 458, 877.
- [88] N. Liu, F. Luo, H. Wu, Y. Liu, C. Zhang and J. Chen, *Adv. Funct. Mater.*, 2008, 18, 1518.
- [89] D. A. Dikin, S. Stankovich, E. J. Zimney, R. D. Piner, G. H. Dommett, G. Evmenenko, S. T. Nguyen and R. S. Ruoff, *Nature*, 2007, 448, 457.
- [90] D. Li, M. B. Muller, S. Gilje, R. B. Kaner and G. G. Wallace, *Nat. Nanotechnol.*, 2008, 3, 101.
- [91] H. Chen, M. B. Müller, K. J. Gilmore, G. G. Wallace and D. Li, *Adv. Mater.*, 2008, 20, 3557.

- [92] C. Wang, D. Li, C. O. Too and G. G. Wallace, *Chem. Mater.*, 2009, 21, 2604.
- [93] Y. Hu, X. Li, D. Geng, M. Cai, R. Li and X. Sun, *Electrochim. Acta*, 2013, 91, 227.
- [94] A. Abouimrane, O. C. Compton, K. Amine and S. B. T. Nguyen, *J. Phys. Chem. C*, 2010, 114, 12800.
- [95] X. Zhao, C. M. Hayner, M. C. Kung and H. H. Kung, *ACS Nano*, 2011, 5, 8739.
- [96] H. Gwon, H. S. Kim, K. U. Lee, D. H. Seo, Y. C. Park, Y. S. Lee, B. T. Ahn and K. Kang, *Energy Environ. Sci.*, 2011, 4, 1277.
- [97] P. Poizot, S. Laruelle, S. Grugeon, L. Dupont and J. M. Tarascon, *Nature*, 2000, 407, 496.
- [98] C. M. Park, J. H. Kim, H. Kim and H. J. Sohn, *Chem. Soc. Rev.*, 2010, 39, 3115.
- [99] J. Cabana, L. Monconduit, D. Larcher and M. R. Palacin, *Adv. Mater.*, 2010, 22, E170.
- [100] L. Ji, Z. Lin, M. Alcoutlabi and X. Zhang, *Energy Environ. Sci.*, 2011, 4, 2682.
- [101] S. M. Paek, E. Yoo and I. Honma, *Nano Lett.*, 2009, 9, 72.
- [102] L. S. Zhang, L. Y. Jiang, H. J. Yan, W. D. Wang, W. Wang, W. G.

- Song, Y. G. Guo and L. J. Wan, *J. Mater. Chem.*, 2010, 20, 5462.
- [103] H. Kim, S.-W. Kim, Y.-U. Park, H. Gwon, D.-H. Seo, Y. Kim and K. Kang, *Nano Res.*, 2010, 3, 813.
- [104] Z. S. Wu, W. C. Ren, L. Wen, L. B. Gao, J. P. Zhao, Z. P. Chen, G. M. Zhou, F. Li and H. M. Cheng, *ACS Nano*, 2010, 4, 3187.
- [105] S. Q. Chen and Y. Wang, *J. Mater. Chem.*, 2010, 20, 9735.
- [106] X. Zhu, Y. Zhu, S. Murali, M. D. Stoller and R. S. Ruoff, *ACS Nano*, 2011, 5, 3333.
- [107] C. T. Hsieh, C. Y. Lin and J. Y. Lin, *Electrochim. Acta*, 2011, 56, 8861.
- [108] M. Zhang, D. Lei, X. Yin, L. Chen, Q. Li, Y. Wang and T. Wang, *J. Mater. Chem.*, 2010, 20, 5538.
- [109] G. Zhou, D. W. Wang, F. Li, L. Zhang, N. Li, Z. S. Wu, L. Wen, G. Q. Lu and H. M. Cheng, *Chem. Mater.*, 2010, 22, 5306.
- [110] J. S. Chen, Z. Wang, X. C. Dong, P. Chen and X. W. Lou, *Nanoscale*, 2011, 3, 2158.
- [111] S. Yang, X. Feng, S. Ivanovici and K. Mullen, *Angew. Chem. Int. Ed. Engl.*, 2010, 49, 8408.
- [112] J. Z. Wang, C. Zhong, D. Wexler, N. H. Idris, Z. X. Wang, L. Q. Chen and H. K. Liu, *Chem. Eur. J.*, 2011, 17, 661.

- [113] S. Yang, X. Feng, L. Wang, K. Tang, J. Maier and K. Mullen, *Angew. Chem. Int. Ed. Engl.*, 2010, 49, 4795.
- [114] S. Yang, X. Feng and K. Mullen, *Adv. Mater.*, 2011, 23, 3575.
- [115] Y. Qiu, K. Yan, S. Yang, L. Jin, H. Deng and W. Li, *ACS Nano*, 2010, 4, 6515.
- [116] A. Yu, H. W. Park, A. Davies, D. C. Higgins, Z. Chen and X. Xiao, *J. Phys. Chem. Lett.*, 2011, 2, 1855.
- [117] N. Zhu, W. Liu, M. Xue, Z. Xie, D. Zhao, M. Zhang, J. Chen and T. Cao, *Electrochim. Acta*, 2010, 55, 5813.
- [118] Z. S. Wu, D. W. Wang, W. Ren, J. Zhao, G. Zhou, F. Li and H. M. Cheng, *Adv. Funct. Mater.*, 2010, 20, 3595.
- [119] S. Stankovich, D. A. Dikin, R. D. Piner, K. A. Kohlhaas, A. Kleinhammes, Y. Jia, Y. Wu, S. T. Nguyen and R. S. Ruoff, *Carbon*, 2007, 45, 1558.
- [120] M. Acik, C. Mattevi, C. Gong, G. Lee, K. Cho, M. Chhowalla and Y. J. Chabal, *ACS Nano*, 2010, 4, 5861.
- [121] D. C. Marcano, D. V. Kosynkin, J. M. Berlin, A. Sinitskii, Z. Z. Sun, A. Slesarev, L. B. Alemany, W. Lu and J. M. Tour, *ACS Nano*, 2010, 4, 4806.
- [122] J. H. Lee, N. Park, B. G. Kim, D. S. Jung, K. Im, J. Hur and J.

W. Choi, *ACS Nano*, 2013, 7, 9366.

[123] J. Ha, S. K. Park, S. H. Yu, A. Jin, B. Jang, S. Bong, I. Kim, Y. E.

Sung and Y. Piao, *Nanoscale*, 2013, 5, 8647.

## **Bibliography**

## 1. International Publications

- 1) Massimiliano Labardi\*, Jihyun Park, Hung Kim Nguyen, Daniele Prevosto, **Chae-Yong Seong**, Aleš Mrzel, Giusy Scalia, “Local dielectric spectroscopy of polyvinylpyrrolidone–Mo<sub>6</sub>S<sub>2</sub>I<sub>8</sub> nanowire composite”, *Journal of Non-Crystalline Solids*, **2013**, 379, 224–228.
- 2) Ji Hyun Park, HyeRan Jo, **Chae-Yong Seong**, Kyung Ho Kim, Ales Mrzel, Giusy Scalia\*, Yung Woo Park, “Investigation of composites of polymers and Mo<sub>6</sub>S<sub>2</sub>I<sub>8</sub> nanowires”, *Physica status solidi a*, **2014**, 211, 1122-1127.
- 3) Seung-Keun Park, **Chae-Yong Seong**, Yuanzhe Piao\*, “A Simple Dip-coating Approach for Preparation of Three-dimensional Multilayered Graphene-Metal Oxides Hybrid Nanostructures as High Performance Lithium-Ion Battery Electrodes”, *Electrochimica Acta*, **2015**, 176, 1182-1190.
- 4) Seung-Keun Park, Seunghee Woo, Sohee Lee, **Chae-Yong Seong**,

Yuanzhe Piao\*, “Design and tailoring of three-dimensional graphene–Vulcan carbon–Bi<sub>2</sub>S<sub>3</sub> ternary nanostructures for high-performance lithium-ion battery anodes”, *RSC Advances*, **2015**, 5, 52687-52694.

5) Seung-Keun Park,<sup>+</sup> **Chae-Yong Seong**,<sup>+</sup> Suyeon Yoo, Yuanzhe Piao\*, “Porous Mn<sub>3</sub>O<sub>4</sub> nanorod/reduced graphene oxide hybrid paper as a flexible and binder-free anode material for lithium ion battery”, *Energy*, **2016**, 99, 266-273. (+Co-first author)

6) Suyeon Yoo, Jeongyeon Lee, Jong Min Kim, **Chae-Yong Seong**, Kwang-dong Seong, Yuanzhe Piao\*, “Well-dispersed sulfur wrapped in reduced graphene oxide nanoscroll as cathode material for lithium–sulfur battery”, *Journal of Electroanalytical Chemistry*, **2016**, 780, 19-25.

7) **Chae- Yong Seong**, Seung-Keun Park, Youngkuk Bae, Suyeon Yoo, Yuanzhe Piao\*, “An acid-treated reduced graphene oxide/Mn<sub>3</sub>O<sub>4</sub> nanorod nanocomposite as an enhanced anode material for lithium ion batteries”, *RSC Advances*, **2017**, 7,

37502–37507.

- 8) Youngkuk Bae, **Chae-Yong Seong**, Suyeon Yoo, Seung-Keun Park, Yuanzhe Piao\*, “Solvothermal Synthesis of a Molybdenum Disulfide/Reduced Porous Graphene Oxide Nanocomposite as a High-Performance Anode Material for Lithium-Ion Batteries”, *Energy Technology*, **2017**, 5, 1-9.
  
- 9) Minyoung Yi, Seung-Keun Park, **Chae-Yong Seong**, Yuanzhe Piao, Taekyung Yu\*, “The general synthesis and characterization of rare earth orthovanadate nano crystals and their electrochemical applications”, *Journal of Alloys and Compounds*, **2017**, 693, 825-831.

## 2. International Conferences

- 1) **Chae-Yong Seong**, Ji Hyun Park, HyeRan Jo, Ales Mrzel and Giusy Scalia\*, “Inorganic nanowires in liquid crystals.”, ILCC (International Liquid Crystal Conference) 2012, Mainz, Germany (August 19–24, 2012).
  
- 2) **Chae-Yong Seong** and Yuanzhe Piao\*, “Hybrid and Flexible Nanocomposite Paper of Porous  $\text{Mn}_3\text{O}_4$  Nanorod/Reduced Graphene Oxide for Lithium Ion Battery Anode.”, PRiME (Pacific Rim Meeting on Electrochemistry and Solid-state Science) 2016, HI, USA (October 2–7, 2016).
  
- 3) **Chae-Yong Seong** and Yuanzhe Piao\*, “Hierarchically Stacked and Porous  $\text{Mn}_3\text{O}_4$  Nanorod/Reduced Graphene Oxide Paper as a Hybrid and Flexible Nanocomposite Anode for Lithium Ion Batteries.”, ACEPS-9 (The 9th Asian Conference on Electrochemical Power Sources) 2017, Gyeongju, (August 20–23, 2017).

### 3. Domestic Conferences

- 1) **Chae-Yong Seong**, Suyeon Yoo, Youngkuk Bae and Yuanzhe Piao\*, “Porous Manganese Oxide Nanorods Dispersed on Reduced Graphene Oxides as a Binder-free Anode Paper for Lithium-Ion Batteries.”, 2015 The Korean Chemical Society Fall Meeting, EXCO, Daegu (October 14-16, 2015).
- 2) **Chae-Yong Seong** and Yuanzhe Piao\*, “Hybrid Nanocomposite Paper of Porous  $Mn_3O_4$  Nanorod/Reduced Graphene Oxide for Lithium Ion Battery Anode.”, 2016 The Korean Electrochemical Society Spring Meeting, Kimdaejung Convention Center, Gwangju, (April 7-9, 2016).

# 국문초록

최근 전기자동차에 대한 관심과 맞물려 리튬이차전지에 대한 관심이 더 높아지고 있다. 리튬이차전지는 양극재, 음극재, 분리막 그리고 전해질로 크게 구성되어 있으며 그 중에서도 높은 용량과 함께 고속 충·방전이 가능한 전극소재개발이 가장 시급한 문제로 대두되고 있다.

그래핀은 탄소로 이루어진 2차원 구조의 물질로써 높은 전기전도도, 높은 비표면적, 우수한 기계적 강도, 뛰어난 화학적 안정성 등 때문에 리튬이차전지 음극소재로 각광을 받고 있다. 그래핀의 이론용량은 ( $782 \text{ mA h g}^{-1}$ ) 그라파이트 ( $372 \text{ mA h g}^{-1}$ ) 비해 약 2배 정도 높으며 화학적인 산화를 통해 다양한 응용이 가능하다.

본 학위 논문에서는 그래핀을 기반으로 한 나노복합체를 리튬이차전지용 음극에 적용한 연구에 대해 보고하였다. 먼저 그라파이트를 산화하여 산화그라파이트를 합성하고 이를 물이나 기타 유기용매에 분산하여 산화그래핀 상태에서 나노복합체를 합성하였다. 첫번째로, 계층적 구조를 가진 1차원 산화망간/그래핀 페이퍼 전극을 진공여과로 제조하는 방법을 제안하였고 이를 리튬이차전지용 음극으로 적용하였다. 100 사이클 후에도  $573 \text{ mA h g}^{-1}$ 의 용량을 유지함으로써 가능성을 확인하였다. 두번째로, 1차원 망가나이트/산처리

산화그래핀을 균일하게 혼합한 후 환원하여 산화망간/산처리 그래핀을 합성한 후 이를 음극에 적용하였다. 산처리 그래핀의 기공을 통해 리튬이온의 원활한 이동이 가능하고 이로 인해 용량 및 충·방전 효율이 향상됨을 확인할 수 있었다. 100 사이클 후에도  $749 \text{ mA h g}^{-1}$ 의 높은 용량을 가짐을 확인하였다. 마지막으로 그래핀 위에 산화주석을 수열합성법으로 증착하여 음극에 활용하였다. 이는 산화주석의 부피팽창에 의한 급격한 용량감소를 그래핀을 호스트물질로 사용하여 완화시킴으로써 사이클 안정성을 확보할 수 있음을 확인하였다. 200 사이클 후에도  $720 \text{ mA h g}^{-1}$ 의 용량을 유지함을 확인하였다.

그래핀 기반의 나노복합체를 합성하고 이를 리튬이차전지용 음극에 적용하여 전기화학적 특성을 평가하였으며 이의 리튬이차전지 응용 가능성을 보여주었다.

**주요어:** 그래핀, 1차원 물질, 산화망간, 산화주석, 망가나이트, 나노복합체, 리튬이차전지.

**학 번:** 2012-22448